

Understanding the interaction of the fundamental Lamb-wave modes with material discontinuity: finite element analysis and experimental validation

Structural Health Monitoring

2022, Vol. 21(2) 640–665

© The Author(s) 2021

Article reuse guidelines:

sagepub.com/journals-permissions

DOI: 10.1177/14759217211007118

journals.sagepub.com/home/shm

Mohammad Ali Fakh¹ , Samir Mustapha¹ ,
Mohammad Harb¹ and Ching-Tai Ng² 

Abstract

The interaction of guided waves with a material discontinuity is not well understood. This study investigates the propagation behavior of the fundamental Lamb-wave modes, the symmetric mode (S_0) and the anti-symmetric mode (A_0), upon interaction with welded joints of dissimilar materials. A plate with an intact AA6061-T6/AZ31B dissimilar joint was employed, and the interaction of the propagating wave with the material interface was scrutinized numerically and validated experimentally. Plane-wave approximation was also adopted to investigate the behavior of the symmetric modes, and its performance was compared to the numerical and experimental results. The effect of the angle of incidence on the reflection, transmission, and mode conversion of the incident modes was analyzed. The study was conducted as the excited Lamb wave propagated from AA6061-T6 to AZ31B (forward), and when the propagation direction was reversed (backward). Different techniques were developed to identify the in-plane and out-of-plane modes from the three-dimensional measurements and to separate wave reflections and transmissions of the joint. The fundamental shear-horizontal guided-wave mode (SH_0 mode) has evolved upon the interaction of the obliquely-incident Lamb-wave S_0 mode with the interface. While the reflection of the SH_0 mode from the joint was found to be well-pronounced, its transmission to the other material is extremely weak. The analytical solution, using plane-wave approximation, was accurate for predicting the behavior of the in-plane modes (S_0 and S_0-SH_0 modes). Despite the peaks appearing at the critical angle, the absolute values of the reflection coefficients of the studied modes have shown similar trends between the forward and the backward propagation directions. The total reflection of the excited wave, from the material interface, was not observed in any condition. The transmission coefficients of the S_0 and A_0 modes are almost constant until reaching very steep incidence angles ($i > 78^\circ$). The results were experimentally validated on an intact AA6061-T6/AZ31B friction-stir-welded joint using an excitation frequency of 200 kHz. Measurements along the transmission and reflection directions were conducted using a three-dimensional scanning laser vibrometer. Experimental results showed very good agreement with both the analytical and the numerical ones.

Keywords

Fundamental Lamb modes, shear-horizontal mode, dissimilar joints, wave reflection, wave transmission, three-dimensional laser vibrometry

¹Laboratory of Smart Structures and Structural Integrity (SSSI), Department of Mechanical Engineering, American University of Beirut, Beirut, Lebanon

²School of Civil, Environmental & Mining Engineering, The University of Adelaide, Adelaide, SA, Australia

Corresponding authors:

Mohammad Ali Fakh, Laboratory of Smart Structures and Structural Integrity (SSSI), Department of Mechanical Engineering, American University of Beirut, Bliss Street, P.O. Box 11-0236, Riad El-Solh, Beirut 1107 2020, Lebanon.

Email: mhf17@mail.aub.edu

Samir Mustapha, Laboratory of Smart Structures and Structural Integrity (SSSI), Department of Mechanical Engineering, American University of Beirut, Bliss Street, P.O. Box 11-0236, Riad El-Solh, Beirut 1107 2020, Lebanon.

Email: sm154@aub.edu.lb

Introduction

The increased demand for higher fuel efficiency in all kinds of mobile vehicles has led to a greater interest in using lightweight materials in their structures.^{1,2} Variants of aluminum and magnesium alloys are being widely used in transportation and aerospace industries due to their light weight and attractive properties, including high specific strength, corrosion resistance, and good formability.^{1,3} Different materials, and due to their specific properties (mechanical, thermal, physical, chemical, etc.), may be more advantageous than others for specific applications or locations within the structure.⁴ For this reason, combinations of dissimilar materials are being inevitably used together to optimize the design from both mechanical and economical perspectives.^{2,4} While fasteners are widely utilized for dissimilar-material joining, welding is still preferred, in the case of metals, to achieve higher productivity and lower costs.⁴ Furthermore, due to the low ductility of magnesium alloys, riveting may induce cracks in the material.¹

Attempts to joining aluminum and magnesium alloys using conventional welding techniques were not very successful.⁵ This is mainly due to the difference in the mechanical, physical, and chemical properties between the two alloy families.¹ Using conventional fusion welding techniques leads to the formation of a thick layer of intermetallic compounds between the two joined materials. This layer is usually brittle, thus leading to considerable weakness in the weld.^{2,5} However, friction stir welding (FSW), which is a modern solid-state welding technique invented in 1991,^{6,7} has proven to be very efficient in joining dissimilar metals.^{4,8} FSW is performed at a temperature below the melting points of the joined metals and does not involve bulk material melting. This improves the mechanical microstructure and properties of the weld and provides several advantages over other welding techniques.⁹ FSW is heavily used in many applications including automotive, marine, railway, and aerospace industries.¹⁰

On the other hand, the availability of structures containing dissimilar joints between different metallic alloys necessitates finding technological solutions for their structural health monitoring (SHM). SHM of critical structures, such as aerospace vehicles, is of high importance to provide a continuous condition assessment and ensure their safety. A wide range of ultrasonic nondestructive evaluation (NDE) techniques has been developed in the last two decades,¹¹ and they have proven to provide precise and reliable results, ranging from simple contact A-scan and C-scan techniques to non-contact air-coupled and laser ultrasound.^{12,13} Ultrasonic guided waves (GWs) are capable of propagating for long distances in simple and complex

curvatures.^{14–16} In particular, Lamb waves (LWs) are GWs that propagate in plate-like structures. LWs can be employed to monitor large sections of structures using distributed transducer networks, without the need for tiresome local examinations.¹⁷ This provides a time and cost-effective inspection solution when dealing with components that are difficult to disassemble for conventional NDE or in-situ inspection of inaccessible regions of the structures.¹⁷ The fundamental anti-symmetric (A_0) and symmetric (S_0) LW modes were proved to be highly sensitive to surface and internal cracking in plates.^{18,19} They have been widely used to develop damage identification algorithms for assessing fatigue cracking,^{20,21} delamination,^{22,23} fiber breakage,²⁴ debonding,^{25,26} cracks/notches,^{27,28} and corrosion.²⁹ As a result, LWs have been commonly used as an essential tool to be implemented in SHM systems toward continuous monitoring of structures.

LWs' potential for assessing defects in FSW has been recently examined by the authors of this article. The assessment of flaws in similar AZ31B FSW magnesium plates was, both experimentally and numerically, scrutinized.⁹ LWs were excited and received using Lead Zirconate Titanate (PZT) transducers placed on both sides of the weld line. After separating the S_0 mode from the complex signals, it was employed to successfully classify wormholes of various severities using an attenuation-based damage index. In Hamade et al.,³⁰ the reflection of the A_0 mode from the material interface in an intact dissimilar AA6061-T6/AZ31B FSW was found to be minimal. This reflection has become significant in the presence of a wormhole within the welded joint. LWs were excited using PZT wafers and received using a scanning laser Doppler vibrometer (LDV). The frequency–wavenumber filtering technique was implemented to separate the wave reflected from the welded joint.

Further experimental and finite element (FE) studies aimed at understanding LWs' propagation through similar and dissimilar welds.³¹ Results have shown that the wave behavior is only affected by the change in elastic properties between the two joined metals, irrespective of the thermo-mechanical changes. Different similar and dissimilar intact FSW plates were used for the study, namely, AA7020-T651/AA7020-T651, AA6060/AA7020-T651, and AA6061-T6/AZ31B welded plates. LWs were actuated and received in the normal incidence direction (perpendicular to the weld interface). No reflections were noticed in both the similar and dissimilar aluminum/aluminum welded plates, while clear reflections were observed in the case of the aluminum/magnesium (AA6061-T6/AZ31B) welded plate. At 200 kHz, the average reflection was calculated to be around 27% of the incident wave, when the wave propagated from AA6061-T6 to AZ31B, and about

35% for the opposite propagation direction. The results were correlated with the measurements obtained from a nano-indentation experiment, where a sharp change in the elastic properties of the base metals was detected in the AA6061-T6/AZ31B welded joint, unlike the other two plates that showed constant elastic properties across the weld zones.

The assessment of FSW joints using LWs requires a thorough understanding of the interaction of the wave modes with the material discontinuity at different incidence directions. This includes reflection, scattering, refraction, and mode conversion. As an example, the amplitude of a transmitted LW through features, such as welds, stiffeners, and bends, can be used to indicate its sensitivity to defects beyond or within those features.³² This clear understanding would allow the integration of LW-based techniques in SHM systems and sensor-network designs in structures containing combinations of dissimilar materials.

Intensive work has been done over the years to understand the propagation behavior of bulk waves.^{33–39} Analytical solutions providing the reflection and transmission coefficients of bulk waves, at normal and oblique incidence and between different types of materials, can be readily found in textbooks.^{40,41} The problem becomes more complex when dealing with GWs due to the need for numerical methods for solving the governing equations.³² Gregory and Gladwell⁴² have developed an analytical solution to determine the reflection of a normally-incident symmetric Rayleigh–Lamb wave from a fixed or free edge of a semi-infinite plate. The energy distribution between the various reflected wave modes was then numerically determined, for a fixed Poisson's ratio, and was analyzed for a range of wavenumbers. Scandrett and Vasudevan⁴³ have addressed an in-depth theoretical study on the propagation behavior of normally-incident Rayleigh–Lamb waves in perfectly bonded dissimilar materials. Using a similar approach as in Gregory and Gladwell,⁴² the authors have presented and analyzed the energy distributions of the reflected and transmitted wave modes over a range of excitation frequencies. Symmetric and anti-symmetric incident fields were studied for different material combinations.

Unlike normal incidence problems, LWs and shear-horizontal (SH) waves cannot be separately analyzed in oblique incidence problems due to the existence of mode conversions between them.⁴⁴ Gunawan and Hirose⁴⁴ analyzed the edge-reflection problem of obliquely incident GWs in a plate using the mode decomposition semi-analytical method. Reflection coefficients of different wave modes were plotted against non-dimensional frequency for various cases of symmetric and anti-symmetric incident Lamb modes. Experimental validation was performed on a steel plate

with different incidence angles showing very good agreement with the numerical results. Wilcox et al.³² have used a semi-analytical finite element (SAFE) method to model the scattering of obliquely-incident GWs from an infinitely-long feature in a waveguide. Transmission and reflection coefficients were calculated for different incidence angles and frequencies. The authors compared their simulation solutions to the experimental data for an adhesively-bonded stiffener. Santhanam and Demirli⁴⁵ have also addressed the reflection of obliquely-incident LWs from the free edge of a plate. Symmetric and anti-symmetric LW incident modes were considered, and the problem was analyzed by orthogonal mode decomposition and by enforcement of traction-free boundary conditions using the collocation method. Energy-based reflection coefficients were determined for different frequency-thickness values. A qualitative experimental validation was performed using PZT transducers, while the authors have commented that only order-of-magnitude estimates of the energy coefficients can be determined using such transducers.

On the other hand, several researchers have tackled the problem of LW scattering and mode conversion from damage and geometric discontinuities. Shen and Giurgiutiu⁴⁶ have developed an analytical predictive tool for GW propagation and damage interaction. A framework for exact two-dimensional (2D) LW solution in the frequency domain was proposed. Wave-damage interaction coefficients (WDICs), determined from a local FE model with non-reflective boundaries, are used to describe scattering and mode conversion from the existing damage. Those WDICs are then coupled with the analytical solution to solve for the total wave-field at the needed sensor location. The solution is finally transformed back into the time domain to provide the predicted sensor measurement. Limiting the needed FE calculations to the local region of the damage bypasses the computational and time demands of a full FE model, for large-scale problems, while still benefiting from FE capabilities for modeling complex damage geometries. Poddar and Giurgiutiu⁴⁷ suggested a new analytical method to compute the scattering of straight-crested LWs from geometric discontinuities, which they called complex modes expansion with vector projection (CMEP). The authors applied CMEP to the problem of a step-like change in the plate's thickness. They verified their results by comparison to the axial-flexural model at low frequencies and to 2D FE analysis at higher frequencies. CMEP achieved a perfect agreement with FE results up to 1.5 MHz.mm with 200-times less computational time. Finally, the authors have suggested techniques for the application of CMEP to damages such as notches, cracks, and delamination. As a continuation of the work, Haider et al.⁴⁸ used CMEP in a global–local analytical method to analyze

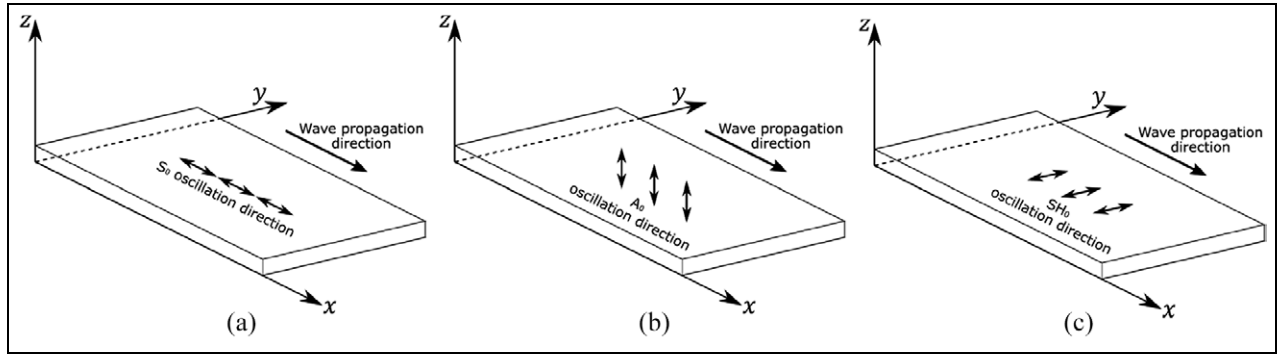


Figure 1. Illustrations of the predominant oscillation directions of the fundamental guided-wave modes: (a) S_0 mode, (b) A_0 mode, and (c) SH_0 mode.

the scattering of A_0 incident waves from an intact and a damaged stiffener within the plate. By comparing the resultant waveforms between the two cases, the crack within the stiffener could be detected. Experiments with selective excitation of straight-crested anti-symmetric LW were conducted for validation, and good agreement in results was attained.

A lot of work, available in the literature, tackles the scattering and interaction of LWs with geometric or structural discontinuity, but there exists very little work tackling their interaction with dissimilar welds. In a recent study,⁴⁹ the behavior of the S_0 and A_0 LWs, upon the normal and oblique interaction with a dissimilar solid joint, was numerically studied. An intact AA6061-T6/AZ31B joint was modeled in “COMSOL Multiphysics”, and LWs’ excitation and propagation were simulated in a three-dimensional (3D) FE environment. Simulation results showed that the S_0 mode was partially converted into the SH_0 mode when obliquely interacting with the material interface. The existing modes (S_0 , A_0 , and S_0 – SH_0) were extracted from their propagation directions, which were determined using Snell’s law for different incidence angles. Reflection and transmission waves were separated from other wave superpositions, and their coefficients were then calculated.

This study expands on the previous work.⁴⁹ An in-depth analysis was performed for a comprehensive investigation of the interaction of LWs with a dissimilar welded joint. A theoretical, numerical, and experimental investigation is presented. Section “Theoretical background and analytical approximation” introduces a general theoretical background about the problem. Identification of the involved GW modes, namely, S_0 , A_0 , and SH_0 modes, based on their oscillation directions and group velocities is explained. Wave-joint interactions including mode conversion, reflection and transmission directions, and critical-angle calculations are investigated. An analytical solution of the in-plane modes based on plane-wave approximation (PWA) is introduced. Section “Finite element modeling” describes

the FE model and measurement details. Section “Experimental validation” describes the samples used for experimental validation, the experimental setup, and data acquisition. Section “Results and discussion” presents and discusses the obtained results. Finally, the last section summarizes the concluding remarks.

Theoretical background and analytical approximation

Wave modes identification

LWs are elastic waves guided by the free top and bottom surfaces of thin plates.¹⁷ The fundamental LW modes are distinguished by their predominant longitudinal and shear-vertical vibrations of particles. A longitudinal wave oscillates the plate particles back and forth in the direction of wave propagation, while a shear-vertical wave oscillates the particles vertically (normal to the plate surface) and perpendicular to the direction of wave propagation. Based on its predominant in-plane longitudinal particle displacement, the fundamental symmetric mode (S_0) can be referred to as the fundamental longitudinal LW mode. Similarly, the fundamental anti-symmetric mode (A_0) can be referred to as the fundamental shear-vertical LW mode. On the other hand, the fundamental SH mode (SH_0) is a GW mode that also propagates in thin plates, with the particles purely vibrating in the horizontal plane (parallel to the plate’s surface) and perpendicular to the wave propagation direction. While in-depth analyses of GW modes’ displacements and shapes can be found in comprehensive textbooks,^{17,41,50} Figure 1 illustrates the predominant vibration directions of the S_0 , A_0 , and SH_0 modes with respect to their propagation direction. In addition to their particle-oscillation directions, different GW modes can be also identified in the measured wave-fields based on their group velocities (c_g).

Considering two aluminum-alloy (AA6061-T6) and magnesium-alloy (AZ31B) plates of 3-mm thickness

Table 1. Mechanical properties of the used materials.

Material	Density (ρ) in kg/m ³	Young's modulus (E) in GPa	Poisson's ratio (ν)
AA6061-T6	2700	69	0.33
AZ31B	1770	45	0.35

joined together, the theoretical group and phase-velocity dispersion curves of the propagating LW modes (mainly A_0 and S_0) were determined using “Wavescope”.⁵¹ Since SH_0 is a non-dispersive mode and based on its theoretical formulation,⁵² both the group and phase velocities of the SH_0 mode were found to be equal to the bulk-wave shear velocity (c_T). The material properties of the joined materials are summarized in Table 1.⁵³

The obtained group-velocity dispersion curves of the LW modes are shown in Figure 2. A typical central frequency of 200 kHz was chosen for LW excitation. The

Table 2. Theoretical group velocities of the existing guided-wave modes at 200 kHz.

Wave mode	c_g (m/s) in AA6061-T6	c_g (m/s) in AZ31B
S_0	5268.7	5280.15
A_0	2980.32	2967.69
SH_0	3099.6	3068.6

frequency was chosen so that only the fundamental modes (A_0 and S_0) are excited in the plate. Table 2 shows the theoretical group velocities of the modes of interest at 200 kHz. The group velocities of the A_0 and S_0 modes are very different, which assures well-separated modes after propagating for some distance. The phase velocities of the fundamental modes at 200 kHz are listed in Table 3.

Figure 3 shows examples of simulated sensor measurements for a 200-kHz GW propagating in the plate

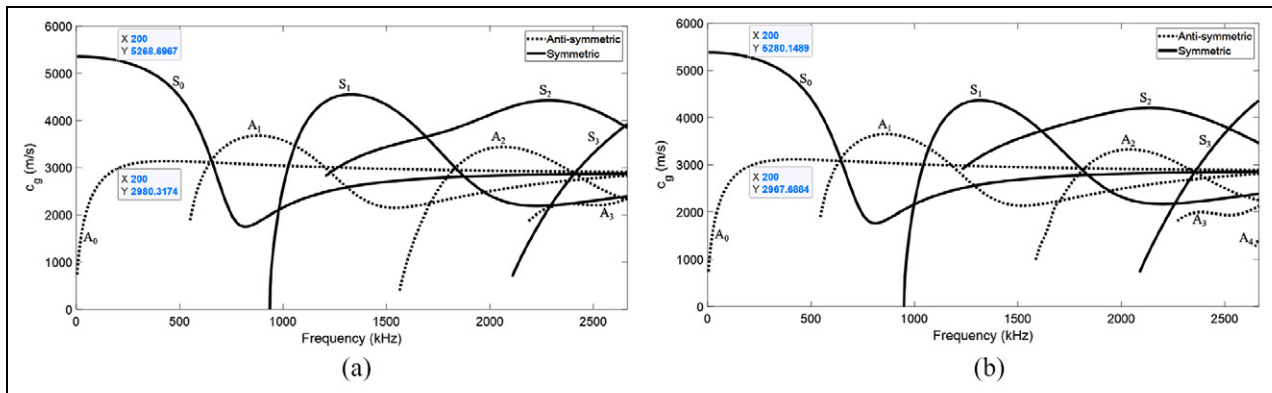


Figure 2. Group-velocity dispersion curves for a plate of 3-mm thickness: (a) AA6061-T6 and (b) AZ31B.

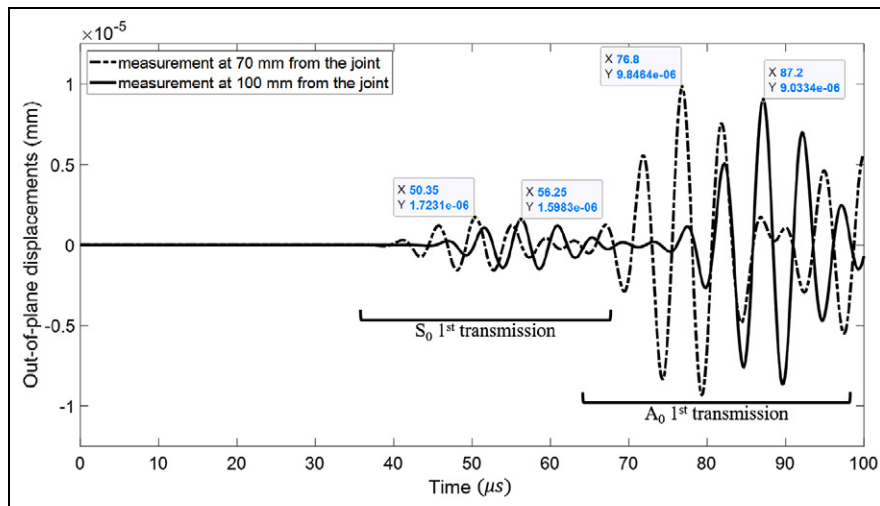


Figure 3. Simulated signals at two different sensing positions to illustrate mode identification.

(details of the FE simulations are explained in section “Finite element modeling”). The wave was excited using a PZT wafer placed on the AA6061-T6 sub-plate. The wave propagated through the intact dissimilar joint and then was captured in the AZ31B sub-plate. Two measurements, taken at two different sensing positions, are shown in Figure 3. The first two wave packets in the signals were identified as the first transmission of the S_0 and A_0 LW modes, respectively. The group velocities of these two modes were calculated using the time-of-arrival of the wave packets, based on the highest peaks (marked in Figure 3). The calculated velocities of the S_0 and A_0 modes were 5084.75 and 2884.62 m/s, respectively, which are in good agreement with the theoretical velocities (in AZ31B) listed in Table 2. Although A_0 is the predominant mode in the out-of-plane displacements, the S_0 mode can still be captured, as shown in Figure 3, due to bending and mode-shape effects.

Wave–joint interactions

Assuming a perfect joint between dissimilar material, ideal transmissions and reflections are expected with no scattering. Upon interaction with the material interface, the energy of the incident modes is distributed among the reflected and transmitted (or so-called refracted) wave modes. Mode conversion is also expected to occur upon the wave interaction with the interface (i.e., the welded joint), thus producing additional modes in the reflected and transmitted portions of the incident wave.⁴¹ The relation between the angles of the incident modes and their corresponding reflected or transmitted modes is defined by Snell’s law⁴⁰ (traction-free boundary condition at the material interface)

$$\frac{c_{p1}}{\sin(\theta_1)} = \frac{c_{p2}}{\sin(\theta_2)} \quad (1)$$

where c_{p1} and c_{p2} are the phase velocities of the incident and reflected/transmitted modes, respectively; and θ_1 and θ_2 are, respectively, the acute angles between the incident or reflected/transmitted modes’ propagation direction and the normal to the material interface.

To differentiate between different angles that will be used throughout this article, incidence angles will be defined as \hat{i} instead of θ_1 , while reflection and transmission angles will be respectively named \hat{r} and \hat{t} instead of θ_2 .

Mode conversion. In the case of oblique incidence, incident-wave modes may convert into other wave modes, at the level of the joint, while being transmitted to the other material or reflected into the same material.⁴¹ Figure 4(a) illustrates the general case of an in-plane longitudinal mode (L_1) incident at a solid-solid

material interface. A portion of the incident L_1 converts into an in-plane shear mode (S) after interacting with the interface. This yields two in-plane modes (L_1 and S_1) reflecting into Material 1, and two other in-plane modes (L_2 and S_2) transmitted into Material 2.

Based on the above, a portion of the incident S_0 wave mode will be converted into the symmetric SH_0 mode when obliquely interacting with the joint.⁵² SH_0 mode would also be generated upon the interaction of the S_0 mode with the plate’s boundaries. This study will focus on the interaction of incident LW modes with dissimilar-material joints; thus, the studied SH_0 mode will be only the mode converted from the incident S_0 wave mode upon its interaction with the joint. This mode will be referred to as S_0 – SH_0 mode in the rest of this article.

On the other hand, since the predominant displacement of the A_0 mode is parallel to the material interface (at both normal and oblique incidence), no other displacement component would be generated upon its interaction with the weld. Thus, the A_0 mode should not undergo any mode conversion under the assumption of a perfect joint.

Critical angles. The critical angle (θ_c) of a wave mode is defined as the largest incidence angle which still results in the refraction of this mode. Beyond this angle ($\theta_1 > \theta_c$), the mode would undergo total internal reflection after interacting with the interface.⁴¹ If the wave mode is excited at its critical incidence angle ($\theta_1 = \theta_c$), it would refract along the material interface, that is, with an angle of refraction $\theta_2 = 90^\circ$. Thus, the critical angle of each mode can be calculated using Snell’s law by replacing θ_2 by 90°

$$\begin{aligned} \frac{c_{p1}}{\sin(\theta_c)} &= \frac{c_{p2}}{\sin(90^\circ)} \\ \Rightarrow \theta_c &= \arcsin\left[\frac{c_{p1}}{c_{p2}}\right] \quad \forall c_{p1} < c_{p2} \end{aligned} \quad (2)$$

If the incident wave mode undergoes conversion at the interface, two critical angles may exist.⁴¹ Referring to Figure 4 (in-plane longitudinal incident mode), upon exciting at the first critical angle (θ_{cL}), L_2 will be refracted along the material interface (L_{int} in Figure 4(b)). Beyond θ_{cL} , the unconverted portion of the incident L_1 would undergo total internal reflection within Material 1, while S_2 keeps refracting into Material 2. If the incidence angle is increased up to the second critical angle (θ_{cS}), if exists, S_2 will be refracted along the material interface (S_{int} in Figure 4(c)), which means no wave will be transmitted into Material 2 anymore. Beyond

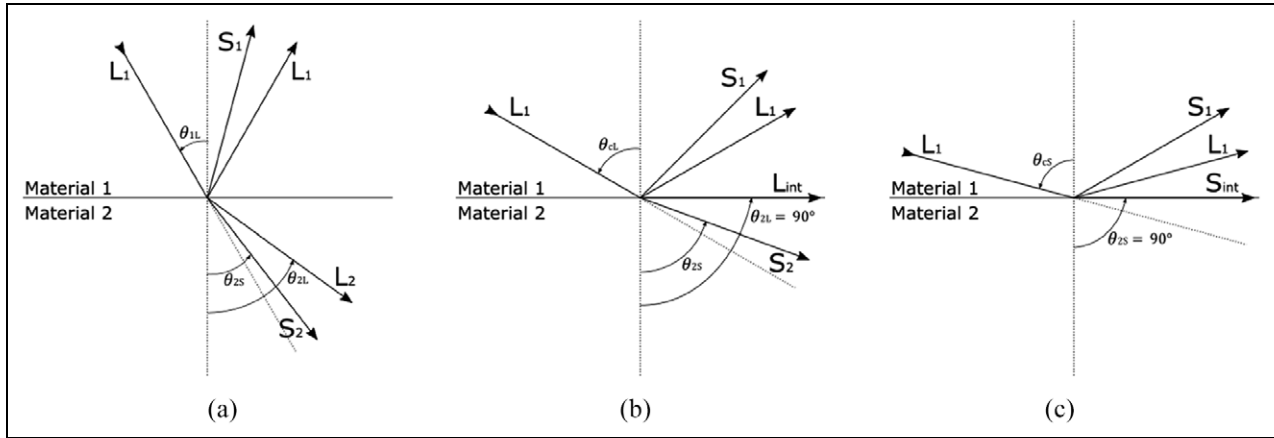


Figure 4. (a) General case of a longitudinal wave incident at a solid-solid material interface, and illustrations of the (b) first critical angle ($\theta_{iL} = \theta_{cL}$) and (c) second critical angle ($\theta_{iL} = \theta_{cS}$).

Table 3. Theoretical phase velocities and critical angles of the existing guided-wave modes at 200 kHz.

Wave mode	c_p (m/s) in AA6061-T6	c_p (m/s) in AZ31B	θ_c (AA6061-T6 to AZ31B)	θ_c (AZ31B to AA6061-T6)
S_0	5327.06	5349.19	84.79°	–
A_0	1990.08	1989.21	–	88.31°
S_0 – SH_0	$c_{p1(S_0)} = 5327.06$ $c_{p2(SH_0)} = 3099.6$	$c_{p2(SH_0)} = 3068.6$ $c_{p1(S_0)} = 5349.19$	–	–

θ_{cS} , the whole incident mode will undergo total internal reflection in Material 1.

In particular, because the incident S_0 mode within this study may convert into the SH_0 mode, two critical angles may exist. The first critical angle is for the transmitted S_0 mode, while the second critical angle is for the transmitted S_0 – SH_0 mode. According to equation (2), the critical angle exists only if the phase velocity of the transmitted wave mode in Material 2 is greater than that of the incident mode in Material 1 (i.e., when propagating from a slower to a faster medium in terms of the phase velocities of the involved modes).

Table 3 summarizes the theoretical phase velocities and critical angles of the modes considered in this study. The second critical angle does not exist for the S_0 – SH_0 mode since the phase velocity of the incident mode (S_0) is always greater than that of the refracted mode (SH_0). Similarly, no critical angle exists for the S_0 mode when the wave propagates from AZ31B to AA6061-T6, as well as for the A_0 mode when the wave propagates from AA6061-T6 to AZ31B.

PWA of in-plane modes

According to Gunawan and Hirose,⁴⁴ when $\omega h/c_T \rightarrow 0$ (where ω is the angular frequency = $2\pi f$; h is half of the plate's thickness = $d/2$; and c_T is the transverse/

shear bulk-wave velocity), the S_0 mode behaves as the longitudinal bulk wave with a constant through-thickness value and a zero out-of-plane value. Under the same condition, the SH_0 mode is reduced to the shear bulk wave which is also constant through-thickness and null in the out-of-plane direction. In other words, when $\omega h/c_T \rightarrow 0$, the amplitudes of the fundamental symmetric modes (S_0 and SH_0 modes) can be determined under the assumption that the plate is in a 2D plane-stress state. This means that the transmission and reflection coefficients of the S_0 and SH_0 modes can be approximated by those of the longitudinal and shear bulk waves, respectively. Gunawan and Hirose⁴⁴ have studied the reflection of obliquely-incident GWs from the free edge of a plate, where they have compared their semi-analytical results to the bulk-wave approximation results. This approximation was found to be accurate at a value of $\omega h/c_T = 1.96$.

Wilcox et al.³² have also confirmed this concept justifying that the mode shapes of the symmetric S_0 and SH_0 modes are almost constant through the plate's thickness at low frequency \times thickness ($f \cdot d$) values, which makes their solutions analogous to longitudinal and transverse bulk waves. The authors have used this analogy as one of the validations of their SAFE approach. Similarly, they compared the results of their SAFE model, for the S_0 and S_0 – SH_0 reflections from

the free edge of a 1-mm aluminum plate in the case of an incident S_0 mode, to explicit analytical solutions of bulk waves.⁵⁴ The comparison was conducted both at different incidence angles and using a constant incidence angle with a variable excitation frequency. Very good agreement of the results was attained up to an $f.d$ value of 1.5 MHz.mm. The authors have commented that such an agreement up to 1.5 MHz.mm cannot be attributed to the plane-stress analogy because the mode shape of the S_0 mode, at such frequencies, contains significant out-of-plane stress. However, the disagreement of the results at $f.d$ values lower than 0.2 MHz.mm was justified by the deterioration of a part of their model's performance (absorbing region) at low frequencies.

In the current work, and for ease of statement throughout the text, this analogy will be named as PWA since the S_0 and S_0 - SH_0 modes are approximated as plane waves propagating in a certain direction with constant mode shapes through the plate's thickness. Based on the mentioned literature results,^{32,44} PWA is expected to be valid for the used $f.d$ value ($f.d = 200 \text{ kHz} \times 3 \text{ mm} = 0.6 \text{ MHz.mm}$) and for both examined materials ($\omega h/c_T \approx 0.61$ for both AA6061-T6 and AZ31B). It should be noted here that PWA can only be applied to the in-plane modes (assumed constant through-thickness, i.e., assumed in a 2D plane-stress condition) and cannot be applied to the case of an incident A_0 mode.

Joseph Rose,⁴¹ in his book "Ultrasonic Guided Waves in Solid Media," provides a matrix formulation for the analytical calculation of transmission and reflection coefficients (vector X), of a harmonic plane-wave incident at a perfect solid-solid interface, as follows

$$MX = a$$

$$X = \text{transpose}([R_L, R_S, T_L, T_S])$$

$$M = \begin{bmatrix} -\cos \hat{r}_L & \sin \hat{r}_S & -\cos \hat{t}_L & \sin \hat{t}_S \\ -\sin \hat{r}_L & -\cos \hat{r}_S & \sin \hat{t}_L & \cos \hat{t}_S \\ k_{1L}(\lambda_1 + 2\mu_1) \cos 2\hat{r}_S & k_{1S}\mu_1 \sin 2\hat{r}_S & k_{2L}(\lambda_2 + 2\mu_2) \cos 2\hat{t}_S & -k_{2S}\mu_2 \sin 2\hat{t}_S \\ -k_{1L}\mu_1 \sin 2\hat{r}_L & -k_{1S}\mu_1 \cos 2\hat{r}_S & -k_{2L}\mu_2 \sin 2\hat{t}_L & -k_{2S}\mu_2 \cos 2\hat{t}_S \end{bmatrix} \quad (3)$$

$$a_L = \begin{bmatrix} -\cos \hat{r}_L \\ \sin \hat{r}_L \\ k_{1L}(\lambda_1 + 2\mu_1) \cos 2\hat{r}_S \\ -k_{1L}\mu_1 \sin 2\hat{r}_L \end{bmatrix} \quad \text{and} \quad a_S = \begin{bmatrix} \sin \hat{r}_S \\ \cos \hat{r}_S \\ -k_{1S}\mu_1 \sin 2\hat{r}_S \\ -k_{1S}\mu_1 \cos 2\hat{r}_S \end{bmatrix}$$

where 1 and 2 are the indices of Material 1 and Material 2, respectively; R and T are the reflection and transmission (refraction) coefficients, respectively; L and S are the indices for longitudinal and shear (transverse) waves, respectively; \hat{r} and \hat{t} are the reflection and transmission (refraction) angles, respectively; k is the wavenumber; λ and μ are the material elastic

constants; a_L or a_S are used if the incident wave is a longitudinal wave or a shear (transverse) wave, respectively; and c_L and c_S are the velocities of the longitudinal and shear (transverse) waves, respectively.

The relations between the material elastic constants and the bulk-wave velocities are given as follows⁴¹

$$\rho c_L^2 = \lambda + 2\mu \quad \text{and} \quad \rho c_S^2 = \mu \quad (4)$$

Thus, the terms containing these constants in equation (3) can be replaced as such

$$\begin{cases} k_L(\lambda + 2\mu) = \frac{\omega}{c_L} (\rho c_L^2) = \omega \rho c_L = 2\pi f \rho c_L \\ k_S \mu = \frac{\omega}{c_S} (\rho c_S^2) = \omega \rho c_S = 2\pi f \rho c_S \\ k_L \mu = \frac{\omega}{c_L} (\rho c_S^2) = \frac{2\pi f \rho c_S^2}{c_L} \end{cases} \quad (5)$$

where ρ is the material density; and ω is the angular frequency ($\omega = 2\pi f$).

For an incident longitudinal wave, the first row in equation (3) is derived from the first boundary condition of particle displacements/velocities, at the interface, in the normal direction as follows⁴¹

$$\begin{aligned} & -A_L^{\text{refl}} \cos \hat{r}_L + A_S^{\text{refl}} \sin \hat{r}_S - A_L^{\text{tr}} \cos \hat{t}_L + A_S^{\text{tr}} \sin \hat{t}_S \\ & = -A_L^{\text{inc}} \cos \hat{r}_L \\ & \Rightarrow -\frac{A_L^{\text{refl}}}{A_L^{\text{inc}}} \cos \hat{r}_L + \frac{A_S^{\text{refl}}}{A_L^{\text{inc}}} \sin \hat{r}_S - \frac{A_L^{\text{tr}}}{A_L^{\text{inc}}} \cos \hat{t}_L \\ & \quad + \frac{A_S^{\text{tr}}}{A_L^{\text{inc}}} \sin \hat{t}_S = -\cos \hat{r}_L \\ & \Rightarrow -R_L \cos \hat{r}_L + R_S \sin \hat{r}_S - T_L \cos \hat{t}_L + T_S \sin \hat{t}_S \\ & = -\cos \hat{r}_L \\ & \Rightarrow \frac{R_L \cos \hat{r}_L}{\cos \hat{r}_L} - \frac{R_S \sin \hat{r}_S}{\cos \hat{r}_L} + \frac{T_L \cos \hat{t}_L}{\cos \hat{r}_L} - \frac{T_S \sin \hat{t}_S}{\cos \hat{r}_L} = 1 \end{aligned} \quad (6)$$

$$\begin{bmatrix} -\cos \hat{r}_L & \sin \hat{r}_S & -\cos \hat{t}_L & \sin \hat{t}_S \\ -\sin \hat{r}_L & -\cos \hat{r}_S & \sin \hat{t}_L & \cos \hat{t}_S \\ k_{1L}(\lambda_1 + 2\mu_1) \cos 2\hat{r}_S & k_{1S}\mu_1 \sin 2\hat{r}_S & k_{2L}(\lambda_2 + 2\mu_2) \cos 2\hat{t}_S & -k_{2S}\mu_2 \sin 2\hat{t}_S \\ -k_{1L}\mu_1 \sin 2\hat{r}_L & -k_{1S}\mu_1 \cos 2\hat{r}_S & -k_{2L}\mu_2 \sin 2\hat{t}_L & -k_{2S}\mu_2 \cos 2\hat{t}_S \end{bmatrix} \quad (3)$$

where A_L^{refl} is the amplitude of the reflected longitudinal wave; A_S^{refl} is the amplitude of the reflected shear (transverse) wave; A_L^{tr} is the amplitude of the transmitted (refracted) longitudinal wave; A_S^{tr} is the amplitude of the transmitted (refracted) shear (transverse) wave; and A_L^{inc} is the amplitude of the incident longitudinal wave.

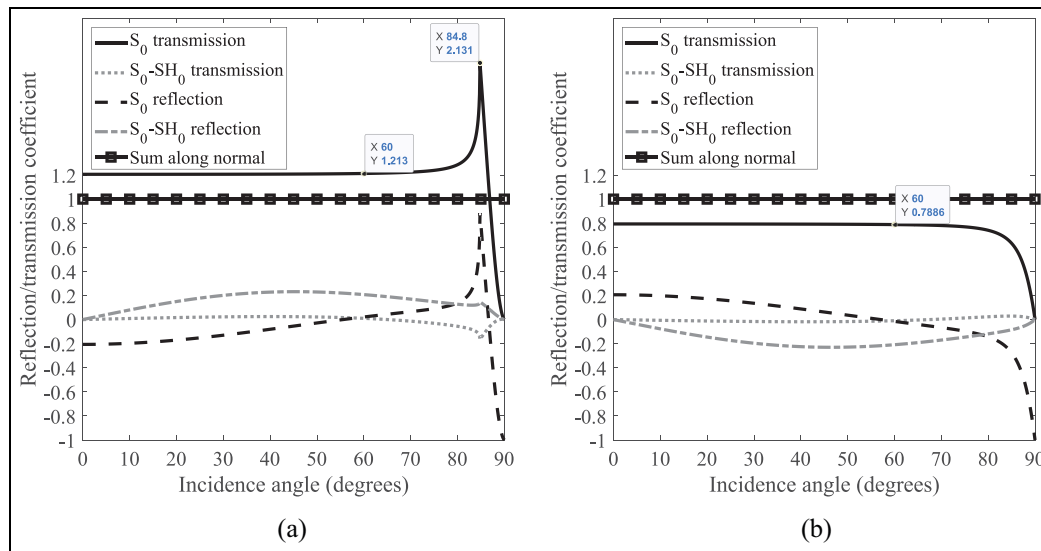


Figure 5. Transmission and reflection coefficients at 200 kHz of the S_0 and S_0 - SH_0 modes using PWA: (a) AA6061-T6 to AZ31B and (b) AZ31B to AA6061-T6.

To apply these formulations for the case of the incident longitudinal S_0 mode, c_L will be replaced by the phase velocity of the S_0 mode (c_{pS_0}), and c_S will be replaced by the phase velocity of the converted S_0 - SH_0 mode (c_{pSH_0}).

Figure 5(a) shows the results for the S_0 incident wave propagating from AA6061-T6 to AZ31B, while Figure 5(b) shows the same results in the opposite propagation direction. The negative sign of the reflection coefficient indicates that the reflected mode is out-of-phase with respect to the incident mode (180° -phase difference). The sum along the normal to the material interface is shown in the figures for verification; this sum should be equal to unity according to equation (6).

Figure 5 can be obtained using equation (3) by calculating X . Each row gives one of the transmission and reflection coefficients, knowing the material properties and the angles. The angles, in turn, can be calculated using Snell's law explained in equation (1).

The transmission coefficient of the S_0 mode stays almost constant from normal incidence ($\hat{i}=0^\circ$) until reaching a steep angle (changes by less than 5% up to $\hat{i}=78^\circ$). The constant value when the wave propagates from AA6061-T6 to AZ31B is about 1.2, while it is about 0.8 in the other propagation direction. Both S_0 transmission and mode conversion drop down to zero at $\hat{i}=90^\circ$ (excitation along the interface), while the S_0 mode's reflection coefficient gives a value of -1 . This indicates that the waves will not be transmitted into the second material in this case.

The abrupt changes in the reflection and transmission coefficients, in the AA6061-T6 to AZ31B propagation (Figure 5(a)), are because the incidence angle is

close to the critical angle. The value of the critical angle in the figure is in good agreement with the value that was calculated in section "Wave-joint interactions" (Table 3). The transmission coefficient of the S_0 mode sharply drops to zero after the critical angle since no S_0 mode will be refracted. Since the second critical angle does not exist for the S_0 - SH_0 mode (Table 3), the total reflection of the incident wave does not occur. Smooth curves appear in Figure 5(b) since no critical angles exist when the S_0 mode propagates from AZ31B to AA6061-T6.

The highest S_0 - SH_0 mode conversion occurs around $\hat{i}\approx 45^\circ$ in both propagation directions. While the transmitted S_0 - SH_0 mode is extremely weak, its reflection reaches significant values of above 20% of the incident S_0 amplitude. The results of the reflection and transmission coefficients, presented in Figure 5, will be discussed in more detail and compared to the numerical and experimental results in section "Transmission and reflection coefficients."

FE analysis was conducted to extend on the application of PWA. The details of the FE model will be explained later within this article. For an excitation frequency of 200 kHz and an incidence angle of $\hat{i}=20^\circ$, the amplitude of the second peak of the refracted S_0 mode, after propagating from AA6061-T6 to AZ31B, was plotted versus the plate's thickness in Figure 6. A measurement was taken at every 0.5 mm in the through-thickness direction after S_0 has propagated for a distance of 85 mm in AA6061-T6 and 80 mm in AZ31B. The amplitudes were normalized based on their highest value for easier analysis. It can be noticed that the maximum amplitude variation through the

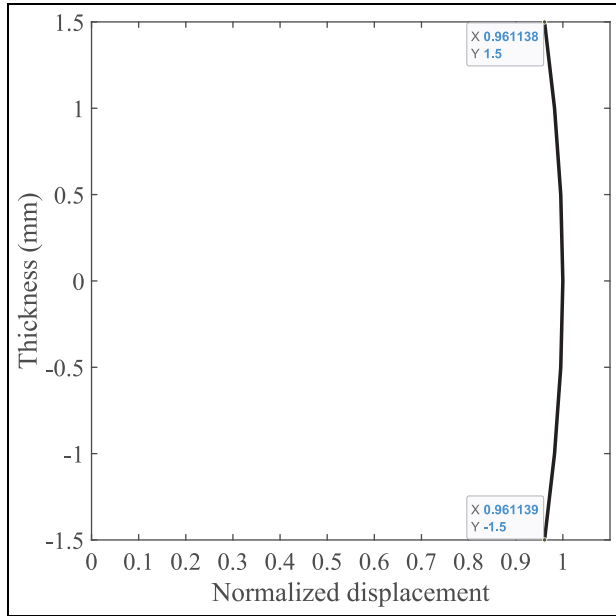


Figure 6. Through-thickness normalized amplitude of the refracted S_0 mode for a wave propagating in the forward direction at $\hat{i}=20^\circ$ (sensor position = 80 mm).

plate’s thickness is around 4%. This confirms the validity of the S_0 mode’s approximation as a plane wave in both materials (AA6061-T6 and AZ31B) at the used $f.d$ value.

FE simulations were also conducted at different excitation frequencies (50–400 kHz) for a LW propagating from AA6061-T6 to AZ31B at a constant incidence angle ($\hat{i}=20^\circ$). The transmission and reflection

coefficients of the S_0 and S_0-SH_0 modes were determined and compared to those calculated using PWA (Figure 7). A good agreement between the FE results and PWA is observed over the studied range of $f.d$ values (0.15–1.2 MHz.mm). Hence, the use of PWA to approximate the symmetric modes is valid within the excited frequency range.

Finite element modeling

“COMSOL Multiphysics” FE software was used to create two adjoining metallic plates of 3-mm thickness and the same size along the common interface (Figure 8). The two plates were joined together to represent a dissimilar-material welded plate assuming a perfect joint. The material properties assigned to each of the sub-plates are listed in Table 1. Homogeneous isotropic linearly-elastic materials were assumed.

Circular piezoelectric (PZT-5H) transducers, 10 mm in diameter and 1 mm in thickness, were modeled based on a solid-mechanics/electrostatics multi-physics solver and were used to excite the LWs. The actuator was placed at 115 mm from the joint’s center, and nine incidence directions were used for excitation, namely, 0° , 10° , 20° , 30° , 40° , 50° , 60° , 70° , and 80° with the normal to the material interface (as shown in Figure 8(a)). The width and length of the two sub-plates were changed, as convenient, based on the position of the transducer and the sensing points upon changing the angle of incidence and propagation directions. Five-cycle Hann-windowed sinusoidal signals, of 200-kHz central frequency and 240-V peak-to-peak voltage, were fed into the poles of the PZT wafer. Forward and backward

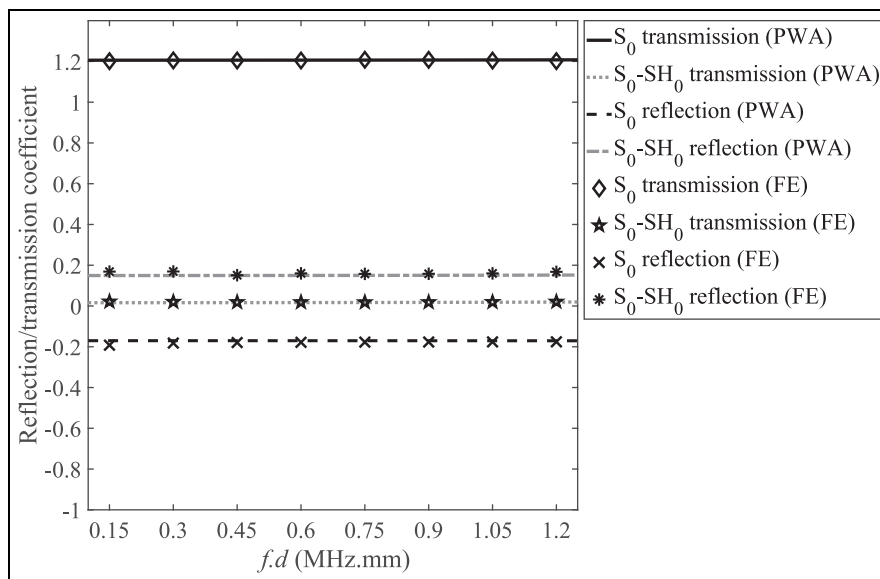


Figure 7. Transmission and reflection coefficients of the S_0 and S_0-SH_0 modes at different excitation frequencies using PWA and FE simulations for a wave propagating in the forward direction at $\hat{i}=20^\circ$.

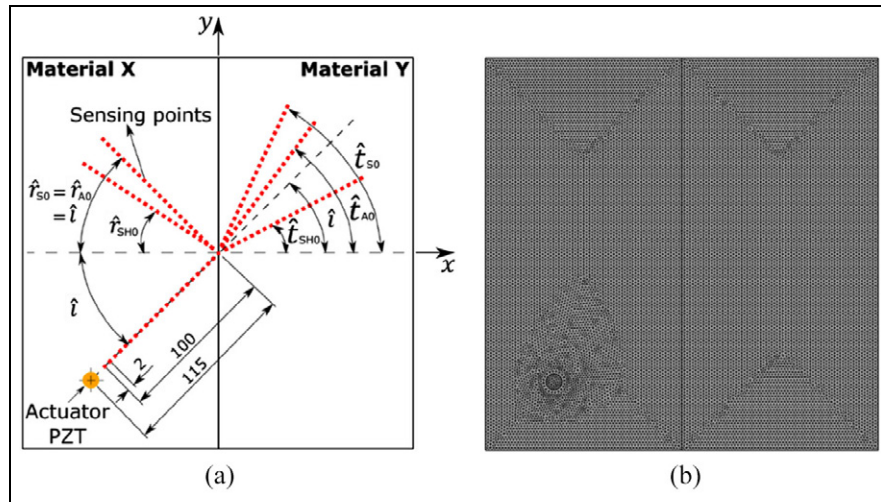


Figure 8. (a) A schematic of the FE model (all dimensions are in mm) and (b) top-view of the meshed FE model ($\hat{i} = 40^\circ$).

directions were simulated (AA6061-T6 to AZ31B and reversed) for each incidence angle. A free tetrahedral mesh was used with a maximum element size of 2 mm (Figure 8(b)). The outer side edges of the plate were assigned low reflecting boundaries to minimize the boundary reflections. Similar analyses were also completed for single-material plates (non-welded AA6061-T6 plate and AZ31B plate) to be used for the separation of interface reflection and transmission wave-fields from other wave superpositions. The separation techniques are explained in sections “Reflection separation” and “ S_0 – SH_0 transmission separation.”

Measurements were taken on all transmission and reflection directions of each of the targeted wave modes. The angles defining those directions are denoted in Figure 8(a) as \hat{i} , \hat{r}_{mode} , and \hat{t}_{mode} for the incidence, reflection, and transmission angles, respectively. The angles were derived based on Snell’s law as discussed in section “Wave–joint interactions.” Using equation (1), given that the phase velocity of the incident modes is constant when propagating in the same material, then their reflecting angles are the same as their incidence angles. The incident wave excited by the PZT wafer contains both S_0 and A_0 modes, therefore, $\hat{r}_{S_0} = \hat{r}_{A_0} = \hat{i}$ as designated in Figure 8(a).

Fifty measurement points (sensors) were chosen along each of the propagation directions and an additional measurement was taken on the material interface (central point). This resulted in a total of 301 measurement points that are allocated on the surface of the plate based on the incidence angle and propagation directions across materials. All the sensors were placed at 2-mm spacing (as seen in Figure 8(a)). They were distributed along a distance of 100 mm before and 100 mm after the interface and along the transmission

and reflection directions of each mode. This will be indicated, later in this article, as -100 to 100 mm in the spatial-time plots of the waves.

Displacements, at the sensing points, in the x -direction (u), y -direction (v), and z -direction/out-of-plane (w) were extracted at a sampling rate of 20 MHz. The collected data were then used to determine the wave-fields related to each mode. The mode extraction, based on the FE and experimental measurements, is discussed in detail in section “Mode extraction.”

Experimental validation

Sample preparations

Two specimens were used for the experimental validation: one non-welded AA6061-T6 plate and another intact friction-stir-welded AA6061-T6/AZ31B plate. The two plates are of $250 \times 250 \times 3$ mm³ dimensions, as shown in Figure 9. The measurements from the non-welded AA6061-T6 plate were used for the separation of reflection and transmission wave-fields, as will be explained later in sections “Reflection separation” and “ S_0 – SH_0 transmission separation.”

Circular PZTs with wrapped electrodes, of 10-mm diameter and 1-mm thickness, were placed in a circular pattern on the surface of the specimens. This has allowed the wave actuation at different incidence angles while keeping a constant distance (along the propagation direction) from the welded joint or the middle line of the plate. The distance from the center of the PZT actuators to the center of the joint was 90 mm. A special template was cut using a laser cutting machine to be used for fixing the PZTs at a constant radius with a

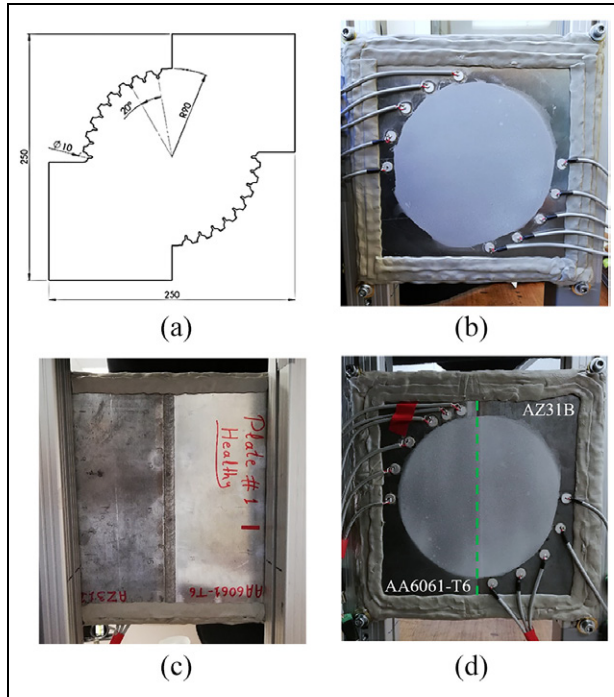


Figure 9. (a) A drawing of the template used for proper PZT placement (dimensions are in mm), and photographs of the specimens used in this study: (b) AA6061-T6 plate, (c) AA6061-T6/AZ31B plate's front-side, and (d) AA6061-T6/AZ31B plate's back-side.

20°-angular distribution (Figure 9(a)). The PZTs were placed at both sides of the joint to excite LWs in both the forward and backward directions. The plate edges were covered by several layers of gummy tapes to dampen the boundary reflections of the excited waves (Figure 9(b) to (d)).

The scanning area was covered by a layer of retro-reflective spray, as shown in Figure 9(b) and (d). The retro-reflective effect reflects the laser beam back to the laser head with minimal scattering, which increases the laser focus and makes it more uniform among the scanned points. This would make the laser measurements less noisy and more reliable.

The healthy condition of the FSW plate was assured by performing a computed tomography (CT) scan of the plate and checking the weld for any damage. The CT scan was performed using a high-resolution CT scanner (Philips iCT 256). A through-thickness cross-sectional CT image of the welded plate is shown in Figure 10. No voids can be seen through the material interface, indicating the intact condition of the joint.

Experiment setup

Figure 11 shows a photo of the system used to acquire the ultrasonic GWs. A Polytec PSV-400 3D scanning

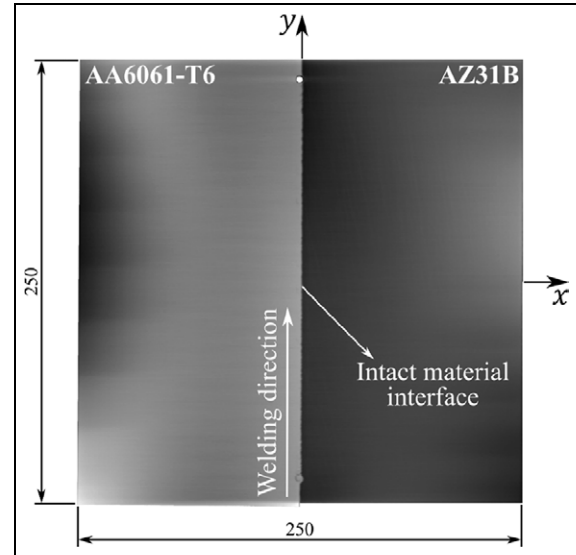


Figure 10. A through-thickness cross-sectional view of the welded test specimen, from a CT scan, showing its intact weld condition. Dimensions are in mm.

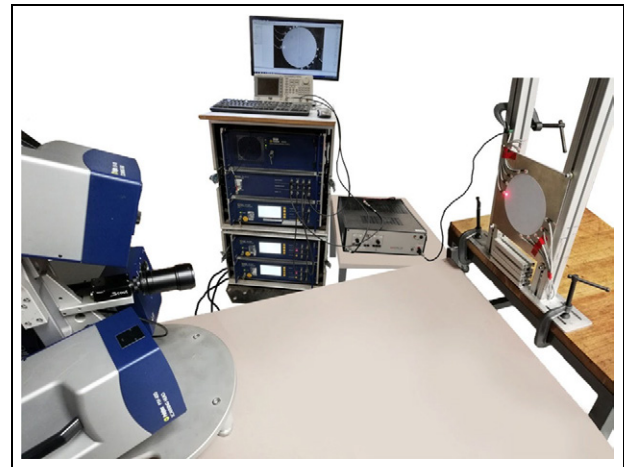


Figure 11. A photo of the experimental setup showing the Polytec PSV-400 3D SLV and its control box, the signal generator, the amplifier, and a testing specimen. The specimen shown in the figure is before using gummy tapes on its edges.

laser vibrometer (SLV) (with three separate laser heads and a data acquisition system) was used to measure the GWs in the testing specimens. Five-cycle Hann-windowed tone burst signals, of 200-kHz central frequency, were used to excite the LWs in the plates. The tone bursts were generated via a signal generator (Tektronix AFG 3021B), amplified up to 240 V peak-to-peak voltage using a power amplifier (Krohn-Hite model 7500), then fed into the piezoelectric transducers. Different incidence angles, varying from 0° to 80° with a step of

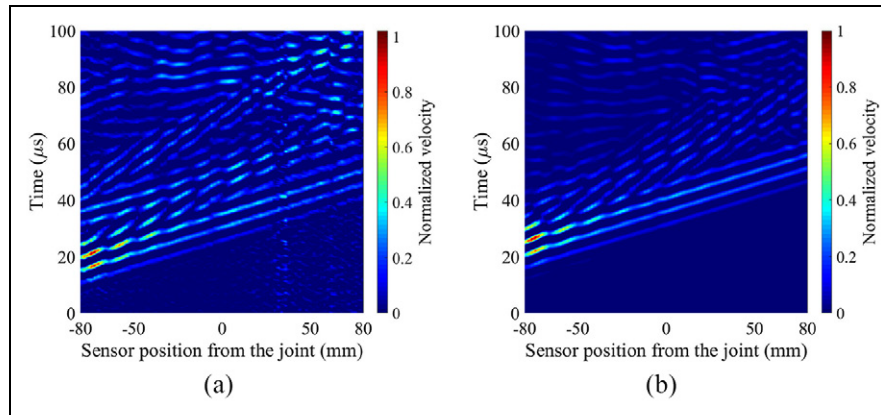


Figure 12. Spatial-time plots of the in-plane normalized velocity field (along the wave propagation direction) measured from the FSW plate, for a wave propagating from AA6061-T6 to AZ31B at $\hat{i}=0^\circ$: (a) before and (b) after using gummy tapes and retroreflective spray.

20° , were used to excite the LWs. Waves were actuated in the forward and backward directions for every incidence angle, while measurements for each actuation were taken using the 3D SLV.

The 3D velocity components were measured at all the reflection and transmission directions of the existing wave modes. Scanning points were defined along the propagation directions with a 2-mm resolution. This is to ensure a high-quality resolution image of the wave propagation. A scanning point was placed at the center of the material interface, while 40 other scanning points were distributed along each of the propagation directions, thus covering a scanning distance of 80 mm on either side of the weld. This is indicated as -80 to 80 mm in the spatial-time plots of the GWs.

To increase the signal-to-noise ratio, 200 time-response measurements were averaged at each scanning point. A low-pass filter was applied to remove the high-frequency noise from the measurements. A sampling rate of 2.56 MHz was used in all experimental measurements.

Figure 12 shows an example of the spatial-time plots of the in-plane normalized velocity fields (along the wave propagation direction) of a line scan from the AA6061-T6/AZ31B plate before and after using the gummy tapes and retroreflective spray. The line scan was made, along the central horizontal line while exciting the zero-incidence-angle PZT. A high percentage of the boundary reflections were absorbed by the gummy tapes, and focused measurements were obtained after using the retroreflective spray, as shown in Figure 12(b).

Results and discussion

Mode extraction

The in-plane displacements/velocities in the x - and y -directions (u and v , respectively), as well as the out-of-

plane displacements/velocities in the z -direction (w) were recorded at all the measurement points. The displacements/velocities (w) correspond mainly to the A_0 mode oscillations (Figure 13(a)). Referring to the schematic diagrams shown in Figure 13(b) and (c), the S_0 and SH_0 wave-fields can be calculated according to equations (7) and (8), respectively

$$U_{S_0} = u * \cos(\phi_{S_0}) + v * \sin(\phi_{S_0}) \quad (7)$$

$$U_{SH_0} = v * \cos(\phi_{SH_0}) - u * \sin(\phi_{SH_0}) \quad (8)$$

where U_m is the displacement field of the mode “ m ”; ϕ_m is the angle between the x -axis and the mode propagation direction (\neq oscillation direction); based on the quadrant in which the sensing points are located and the wave’s propagation direction, ϕ of a certain mode varies according to the following geometrical cases: geometrical case 1: first or third quadrant, a wave propagating from left to right: $\phi_m = \theta_m$, geometrical case 2: first or third quadrant, a wave propagating from right to left: $\phi_m = 180^\circ + \theta_m$, geometrical case 3: second or fourth quadrant, a wave propagating from left to right: $\phi_m = -\theta_m$, and geometrical case 4: second or fourth quadrant, a wave propagating from right to left: $\phi_m = 180^\circ - \theta_m$; and θ_m is the acute angle between the propagation direction of the mode “ m ” and the normal to the material interface.

Although circular-crested waves are obtained by PZT actuation, determining the modes of interest along one propagation direction, as illustrated in Figure 13, proved to be an efficient simplification of the problem to be similar to an obliquely-incident straight-crested LW propagation.

Signals collected from all the sensing points along a given measurement direction can be plotted in the spatial-time domain. This can be achieved by accumulating all the vertical time plots of the signals side-by-side along the spatial axis (horizontal axis). Figure 14(a),

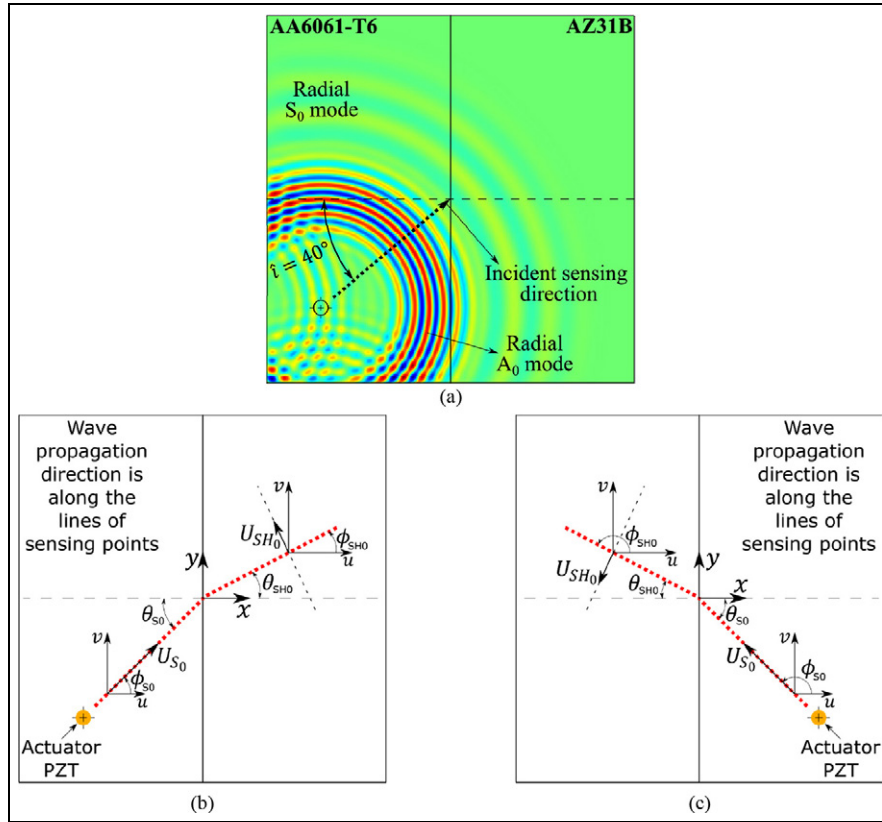


Figure 13. (a) Sample out-of-plane displacements on the surface of the plate for a wave propagating in the forward direction at $\hat{i} = 40^\circ$, and two illustrating examples of S_0 and SH_0 wave-field calculations: (b) geometrical case 1 and (c) geometrical case 4.

Table 4. FE and experimentally obtained group velocities of the LW modes for a wave propagating in the forward direction at $\hat{i} = 20^\circ$.

Measurement	FE		Experimental	
	c_g (m/s) in AA6061-T6	c_g (m/s) in AZ31B	c_g (m/s) in AA6061-T6	c_g (m/s) in AZ31B
S_0	5311.5	5335	5297.9	5311.5
A_0	2951.6	2975.9	3036.6	2829.8

FE: finite element.

(c), and (e) shows the wave-fields obtained using the FE simulations for the wave propagating in the forward direction, at $\hat{i} = 20^\circ$, for the S_0 , A_0 , and SH_0 modes, respectively. Different modes were identified based on their measurement directions and velocities as discussed earlier. Furthermore, Figure 14(b), (d), and (f) shows similar results obtained from the experimental analysis. A good agreement was evident between the results of the FE simulations and the experiments. The obtained average group velocities of the S_0 and A_0 modes are summarized in Table 4.

It was observed that there were some weak boundary reflections in the experimental measurements;

however, they are almost fully suppressed in the FE results due to the use of low reflecting boundaries. The S_0 - SH_0 transmission did not appear clearly in Figure 14(e) due to its low amplitude when compared to the other wave-fields propagating in the plate (less than one-tenth of S_0 amplitude). Experimentally, the S_0 - SH_0 transmission did not appear in Figure 14(f) since it is extremely weak. The separation of the S_0 - SH_0 transmission is discussed further in section “ S_0 - SH_0 transmission separation.”

The experimental measurements were collected using different actuators; therefore, experimental data were normalized. The A_0 wave-fields (along the incidence,

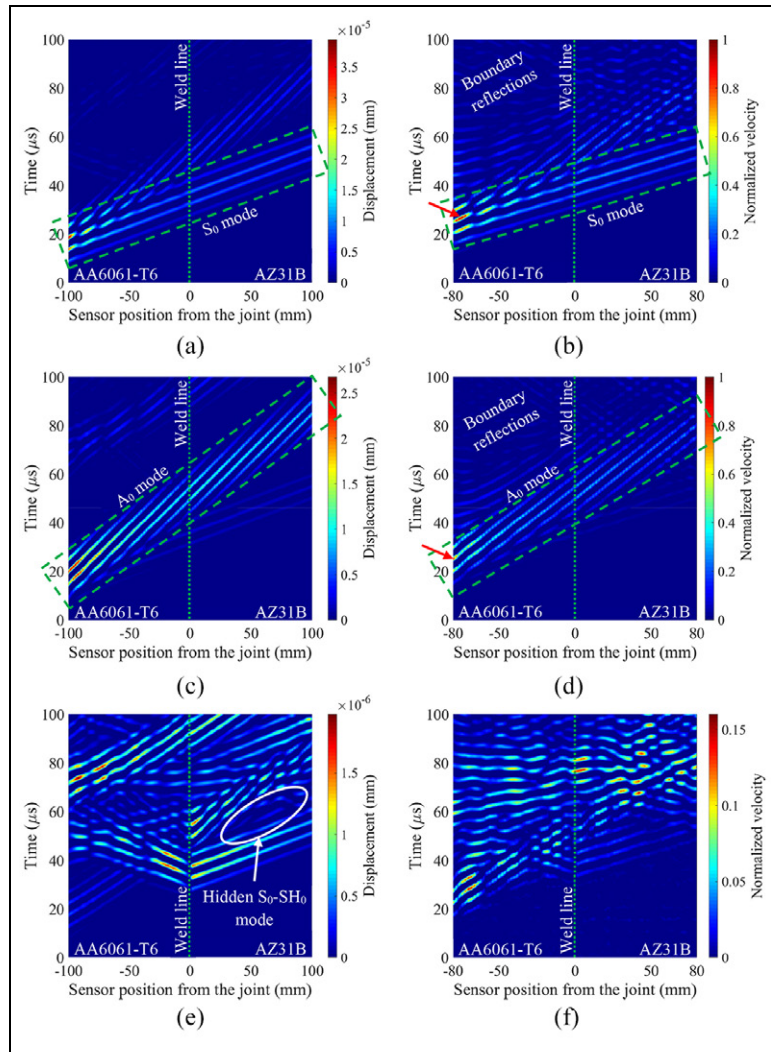


Figure 14. Spatial-time plots of the simulated and experimental wave-fields, along the incidence and transmission directions of different modes, for a wave propagating in the forward direction at $\hat{i} = 20^\circ$: (a) FE U_{S_0} , (b) experimental U_{S_0} , (c) FE U_{A_0} , (d) experimental U_{A_0} , (e) FE $U_{S_0-SH_0}$, and (f) experimental $U_{S_0-SH_0}$.

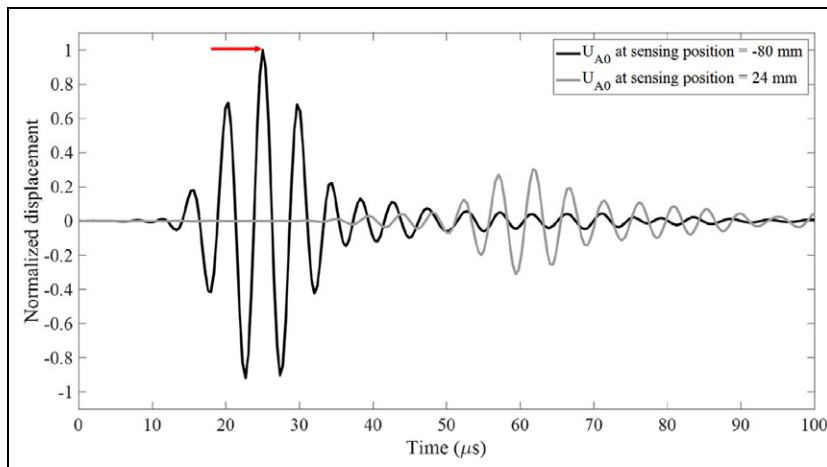


Figure 15. Typical normalized experimental raw signals for U_{A_0} at two different sensing positions.

transmission, and reflection directions) were normalized to the peak value of the first transmission along the incidence direction (indicated by the red arrow in Figure 14(d)). The S_0 and the S_0 - SH_0 measurements were normalized using the peak value of the first transmission of the S_0 measurement along the incidence direction (indicated by the red arrow in Figure 14(b)). Figure 15 shows an example for the U_{A_0} signal (measured in the out-of-plane direction) at the first sensing point (sensor position = -80 mm) and at another sensing point (sensor position = 24 mm). Both signals are part of the wave-field shown in Figure 14(d). The red arrow indicates the peak value in the U_{A_0} wave-field, which was used to normalize all other signals of the wave-field of Figure 14(d).

Reflection separation

Figure 16(a) shows the FE simulation of the S_0 wave-field measured along the reflection direction, for a wave propagating in the forward direction at $\hat{i}=20^\circ$. The waves measured at those sensing locations are the superposition of the direct transmissions from the actuator, boundary reflections, and reflections from the weld region. It is critical to separate the reflections caused by the presence of the material interface/discontinuity.

To separate interface reflections, measurements from the same actuator-sensor configurations were recorded in a single material for the same plate size. The wave-fields measured at the reflection directions (e.g., Figure 16(b)) were then subtracted from the dissimilar-material reflection wave-fields (e.g., Figure 16(a)). The obtained fields are those resulting from the waves' interactions with the dissimilar-material interface (e.g., Figure 16(c)). To isolate the reflections in AA6061-T6 to AZ31B measurements, AA6061-T6 single-material measurements should be subtracted. Similarly, to isolate reflections in the opposite propagation direction, AZ31B single-material measurements are to be used. Equation (9) summarizes the followed reflection separation method for an incident wave propagating from Material X to Material Y

$$U_{R(X/Y)} = U_{RD(X/Y)} - U_{RD(X/X)} \quad (9)$$

where $U_{R(X/Y)}$ is the wave-field, reflected from the material interface, from an incident wave propagating from Material X to Material Y at an angle of incidence \hat{i} ; $U_{RD(X/Y)}$ is the wave-field, measured along the reflection direction, from an incident wave propagating from Material X to Material Y at an angle of incidence \hat{i} ; and $U_{RD(X/X)}$ is the wave-field, measured along the reflection direction, from an incident wave propagating from Material X to Material X at an angle of incidence \hat{i} .

Figure 16(c) shows a clear reflection field of the S_0 mode. This reflection has an average group velocity of 5333 m/s, which is in good agreement with the AA6061-T6 theoretical value presented in Table 2 (5268.7 m/s). The separated reflection fields of the other modes (A_0 and S_0 - SH_0) of the same simulated wave are presented in Figure 17. As mentioned earlier, SH_0 was not significant before the wave interaction with the material interface; thus, its noticeable appearance in the reflection field is due to S_0 - SH_0 conversion upon S_0 interaction with the joint.⁵² This is also clear based on the amplitude of the SH_0 mode in the reflected field (Figure 17(b)), which is higher than its amplitude in the incident field (Figure 14(e)). The average group velocities of the obtained A_0 and SH_0 reflections were determined to be 3062 and 3094 m/s, respectively, and they are both close to the theoretical values shown in Table 2 (2980.32 and 3099.6 m/s, respectively).

The same procedure was applied for the experimental measurements to separate interface reflections from other wave superpositions. The separated reflection fields from experimental measurements were not as clear as those obtained from the FE simulations, which is expected. Figure 18 presents the experimental measurements of the S_0 mode along its reflection direction for an incident wave propagating in the forward direction at $\hat{i}=20^\circ$ (Figure 18(a)), and similarly in the AA6061-T6 single-material plate (Figure 18(b)). After subtracting these two wave-fields, the wave-field in Figure 18(c) was obtained. The reflection field of the S_0 mode can be identified as shown in the figure. It has an average group velocity of 5120 m/s, which has good agreement with the AA6061-T6 theoretical value presented in Table 2 (5268.7 m/s).

It should be noted here that several steps were taken during the experiments to minimize all possible differences between measurements from two different specimens including placement of PZTs, soldering, and connections. The retroreflective spray and gummy tapes were made as uniform and consistent as possible between the two plates. The two plates were placed at the same position and height with respect to the laser, and a precise and careful calibration of the 3D SLV was performed to have similar and accurate measurement positions. Data were normalized to account for differences between different actuator PZTs and bonding quality. Despite all this, errors still existed due to unavoidable operational and environmental variations.

S_0 - SH_0 transmission separation

The measured S_0 - SH_0 transmission along its expected propagation direction was noticed to have a low amplitude when compared to the other measured wave-fields

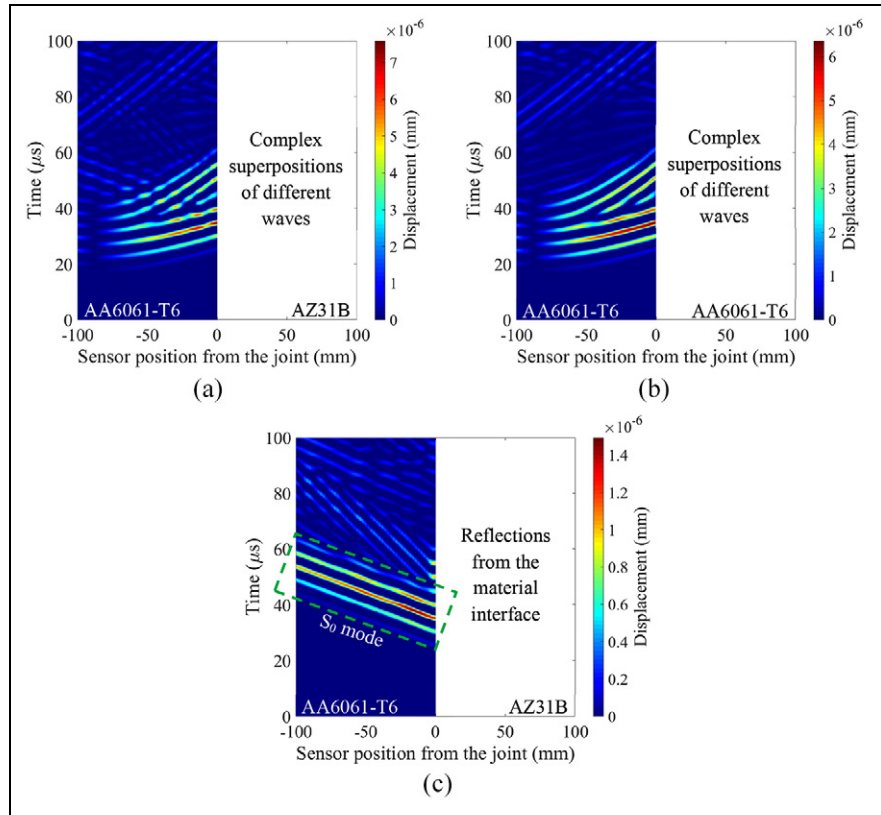


Figure 16. Separation of the S_0 reflection; FE simulation measurements along S_0 reflection direction, for a wave propagating in the forward direction at $i = 20^\circ$: (a) S_0 reflection wave-field measured in the AA6061-T6/AZ31B plate, (b) S_0 reflection wave-field measured in the AA6061-T6 plate, and (c) S_0 reflection computed by subtracting the wave-field shown in (b) from the wave-field shown in (a).

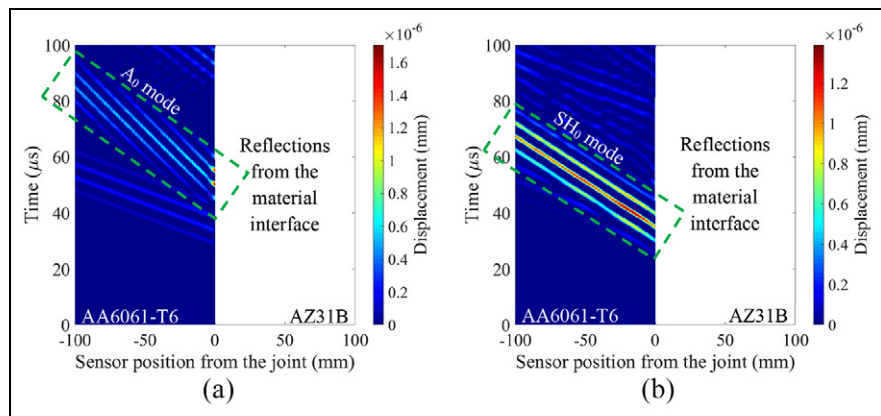


Figure 17. Separated A_0 and S_0-SH_0 reflection fields; FE simulation measurements along their respective reflection directions, for a wave propagating in the forward direction at $i = 20^\circ$: (a) A_0 reflection and (b) S_0-SH_0 reflection.

on the same plate. It was found that this mode is masked by other transmissions and reflections, as shown in Figure 14(e) and (f). Therefore, a separation procedure was established to extract the transmitted/reflected S_0-SH_0 mode.

In the reflection separation (section “Reflection separation”), the wave-fields measured along the reflection directions would have both propagated only in Material X, which makes their direct subtraction a reasonable solution. The wave-field measured along the

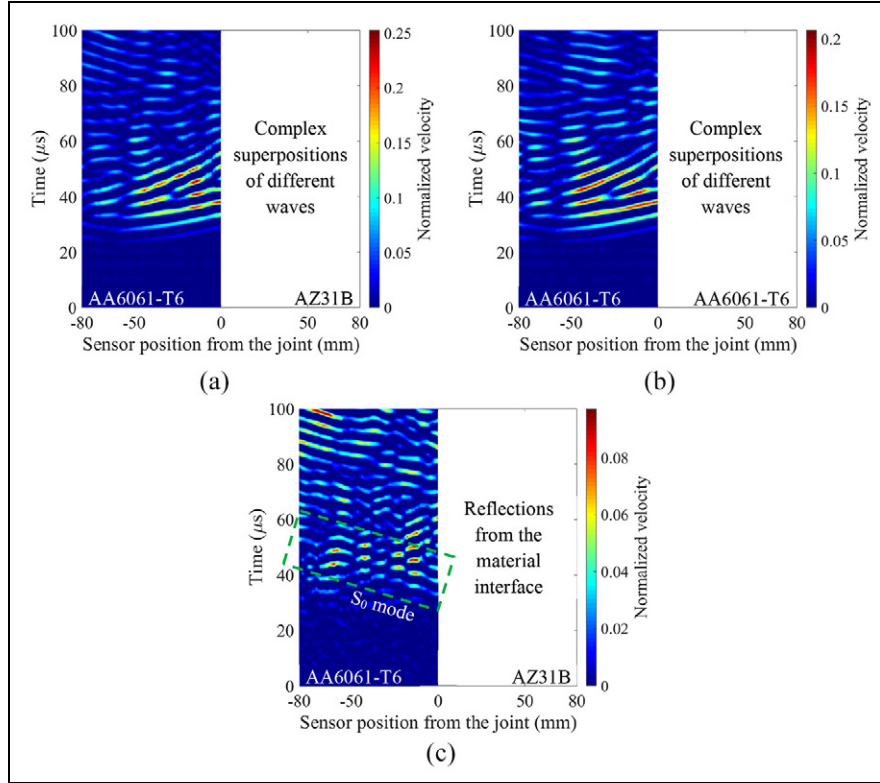


Figure 18. Separation of the S_0 reflection; experimental measurements along S_0 reflection direction, for a wave propagating in the forward direction at $\hat{i} = 20^\circ$: (a) S_0 reflection wave-field measured in the AA6061-T6/AZ31B plate, (b) S_0 reflection wave-field measured in the AA6061-T6 plate, and (c) S_0 reflection computed by subtracting the wave-field shown in (b) from the wave-field shown in (a).

S_0 - SH_0 transmission direction, across a dissimilar joint, would have passed from Material X to Material Y, while in a single-material plate, it would have propagated only in Material X. To account for the amplitude variation between different materials, the single-material wave-field was normalized to that of dissimilar materials before subtraction. Given that the first wave-pack was noticed to be common between the two subtracted wave-fields (Figure 19(a) and (b)), the amplitude of the third obvious peak in this wave-pack was used for amplitude normalization (other peaks can be used for normalization). This procedure is described as follows

$$U_{S_0-SH_0(X/Y)} = U_{SH_0D(X/Y)} - a \times U_{SH_0D(X/X)} \quad (10)$$

where $U_{S_0-SH_0(X/Y)}$ is the refracted S_0 - SH_0 wave-field, converted from the S_0 mode of an incident wave propagating from Material X to Material Y at an angle of incidence \hat{i} ; $U_{SH_0D(X/Y)}$ is the SH_0 wave-field, measured along the S_0 - SH_0 transmission direction, from an incident wave propagating from Material X to Material Y

at an angle of incidence \hat{i} ; $U_{SH_0D(X/X)}$ is the SH_0 wave-field, measured in the same direction as $U_{SH_0D(X/Y)}$, from an incident wave propagating from Material X to Material X at an angle of incidence \hat{i} ; and a is the coefficient that normalizes the amplitudes of $U_{SH_0D(X/X)}$ to those of $U_{SH_0D(X/Y)}$, determined from a chosen peak of the first wave-pack (third peak in this case) and at a chosen sensor position.

Similarly, the time of arrival of the wave-pack, considered for normalization, is a bit different between the two wave-fields due to propagation in different materials. This time-shift would have been more obvious if the group velocities of the studied materials were not close in values (refer to Table 2). The time-shift increases with the propagation distance and, hence, differs from one sensor position to another. Therefore, time-alignment should also be applied to $U_{SH_0D(X/X)}$, at each sensor position, before subtraction.

Figure 19 illustrates the separation of the S_0 - SH_0 transmission for the wave simulation of an incident wave propagating in the forward direction at $\hat{i} = 20^\circ$.

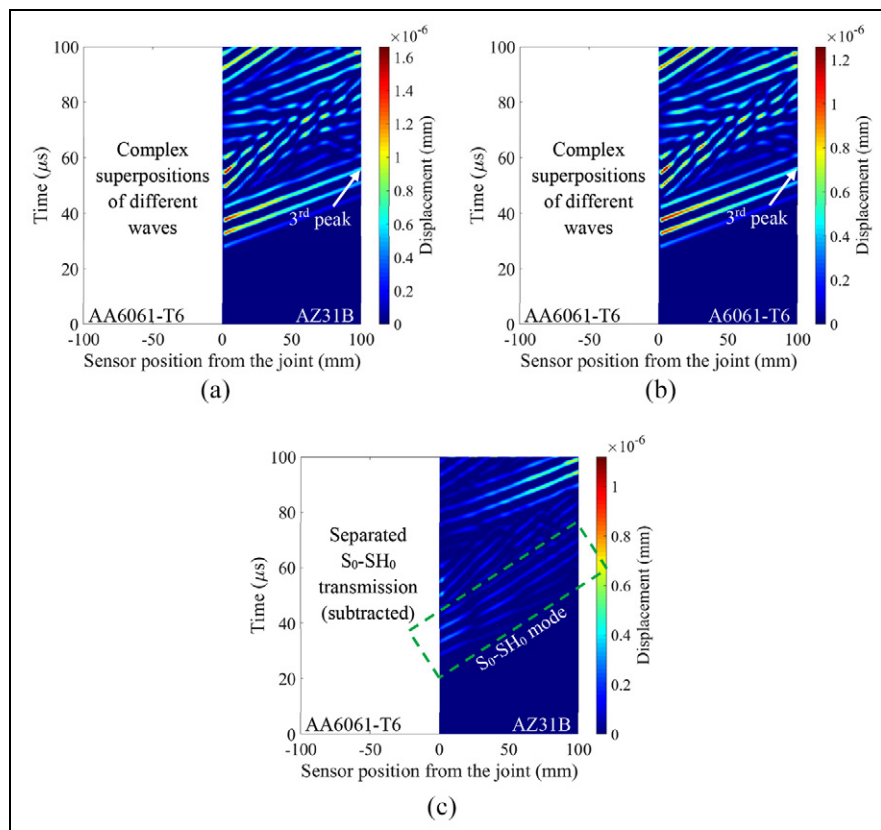


Figure 19. Separation of the S_0 - SH_0 transmission; FE measurements along S_0 - SH_0 transmission direction, for a wave propagating in the forward direction at $\hat{i}=20^\circ$: (a) SH_0 transmission wave-field measured in the AA6061-T6/AZ31B plate, (b) SH_0 transmission wave-field measured in the AA6061-T6 plate, and (c) S_0 - SH_0 transmission computed by subtracting the wave-field shown in (b) from the wave-field shown in (a), based on equation (10).

The average group velocity of the obtained S_0 - SH_0 transmission is 3021 m/s, which is very close to the theoretical value presented in Table 2 (3068.6 m/s).

When applying the same separation method to the experimental measurements, the refracted S_0 - SH_0 mode was very weak to appear. This agrees with both the PWA results (section “PWA of in-plane modes”) and the FE results.

Attenuation curves

The attenuation curve provides information about the change in the amplitude of the propagating wave with distance. Attenuation of LW modes occurs due to multiple possible mechanisms including dispersion, beam divergence, material damping, scattering, and leakage into a neighboring medium.⁵⁵ Investigating the attenuation behavior across multiple media would allow for a better understanding of LW propagation from one

solid medium to another along with the underlying phenomena.

Attenuation in single-material plates (isotropic and non-welded) is not affected by the incidence angle since the material interface does not exist. Thus, the curves determined from multiple experimental measurements (at multiple incidence angles) in the AA6061-T6 plate were averaged to have one single reference and avoid experimental variations between different single-material recordings. Figure 20 shows the experimental S_0 attenuation curves when propagating in the AA6061-T6 plate (for the wave’s first peak) and when propagating in the forward direction in the welded plate (first peak; $\hat{i}=0^\circ$). Upon crossing the material interface (around sensor position ≈ 0), the wave amplitude experiences a sudden jump before it continues in the normal attenuation behavior. This increase in amplitude may indicate that the wave-field is amplified when passing from a stiffer medium (AA6061-T6) to a softer

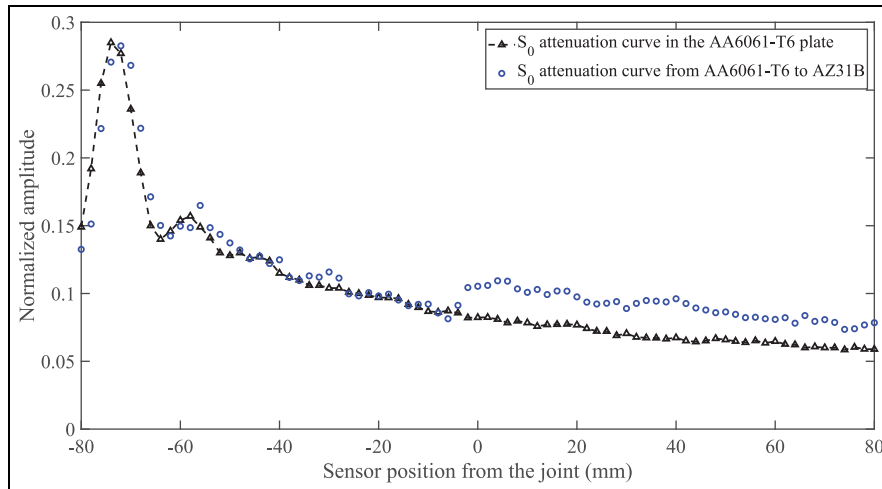


Figure 20. Experimental S_0 -mode attenuation curves in both the AA6061-T6 plate (averaged from all incidence angles; first peak) and the AA6061-T6/AZ31B plate (forward direction; $\hat{i} = 0^\circ$; first peak).

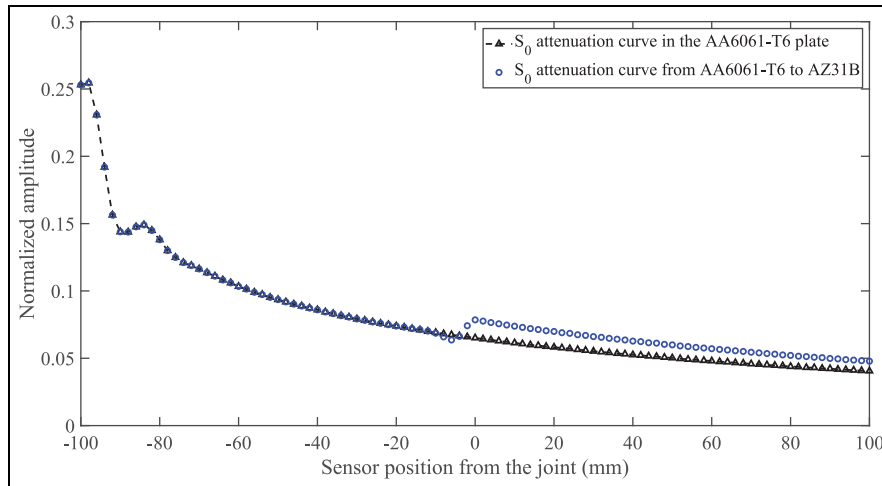


Figure 21. FE S_0 -mode attenuation curves in both the AA6061-T6 plate ($\hat{i} = 0^\circ$; first peak) and the AA6061-T6/AZ31B plate (forward direction; $\hat{i} = 0^\circ$; first peak).

medium (AZ31B). Figure 21 shows the FE results of the same case. Similar conclusions and observations can be drawn from Figure 21, while more data consistency is obvious, due to the absence of possible experimental errors and noise.

Figure 22 shows the experimental and FE attenuation curves of the backward propagation direction (third peak; $\hat{i} = 0^\circ$) as compared to that in the AZ31B single-material plate (non-welded). Unlike the amplitude amplification in the forward direction, the wavefield showed a sudden drop in amplitude upon passing from a softer medium (AZ31B) to a stiffer one (AA6061-T6). The variation between the experimental and FE attenuation curves at their start is because the sensing points in the FE model start at “sensor

position = -100 mm,” while they start at “sensor position = -80 mm” in the experiments (in addition to the difference in the actuator position).

A sinusoidal variation in the S_0 amplitude is evident at the beginning of the attenuation curves of the first peak (Figures 20 and 21); however, this variation increases significantly in the attenuation curves based on the third peak (Figure 22). This oscillation pattern indicates that the S_0 mode was not fully converged. This instability can be explained by two inter-related phenomena, namely, LW dispersion into two different modes of different velocities (A_0 and S_0), and the superpositions between the two modes before their complete separation. To understand these two phenomena, the experimental S_0 spatial-time plots at $\hat{i} = 0^\circ$ are shown in

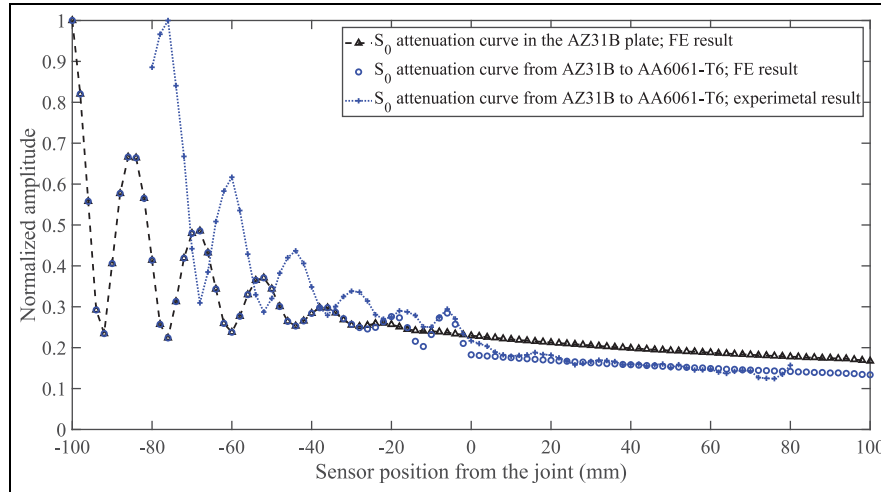


Figure 22. S_0 -mode attenuation curves in both the AZ31B plate (FE result; $\hat{i}=0^\circ$; third peak) and the AA6061-T6/AZ31B plate (FE and experimental results; backward direction; $\hat{i}=0^\circ$; third peak).

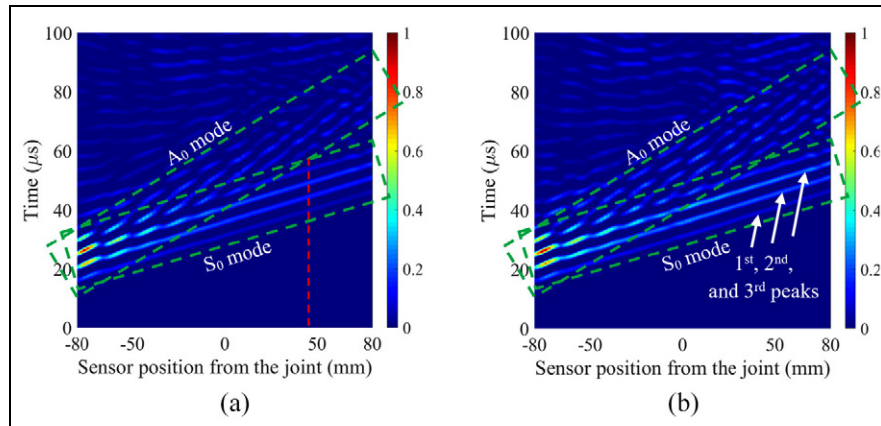


Figure 23. Experimental S_0 -mode spatial-time plots in both the AA6061-T6 plate and the AA6061-T6/AZ31B plate (forward direction; $\hat{i}=0^\circ$): (a) AA6061-T6 and (b) AA6061-T6 to AZ31B.

Figure 23. The two LW modes are identified on the figures, illustrating that the complete separation between the two modes did not occur before about 45 mm from the center of the plate (dashed-red line). The separation of the two modes (dispersion) and the superposition between them while separating have both led to the sinusoidal shape that can be seen in the attenuation curves. It can be also noticed from Figure 23 how the A_0 mode separates from the first peak of the S_0 mode first (sensor position ≈ -50 mm), then it separates from the second peak at a later stage (sensor position ≈ -25 mm), and finally from the third peak approximately at the center of the plate. This explains why the sinusoidal variation lasts for different propagation distances between the attenuation curves of different peaks. Furthermore, the disturbance in the attenuation curves, just before the material interface (sensor

position ≈ 0 mm), is due to the superposition of the incident S_0 mode with its reflection from the material interface.

Transmission and reflection coefficients

The transmission and reflection coefficients of the wave modes were determined through a direct comparison of the amplitudes of the transmitted and reflected fields with the transmissions of the wave in the incidence medium (single-material propagation). Equations (11) and (12) were respectively used to compute the transmission and reflection coefficients of both the A_0 and S_0 modes. The SH_0 mode is a conversion from the S_0 mode; therefore, the transmission and reflection coefficients of the S_0 – SH_0 mode were determined using equations (13) and (14), respectively

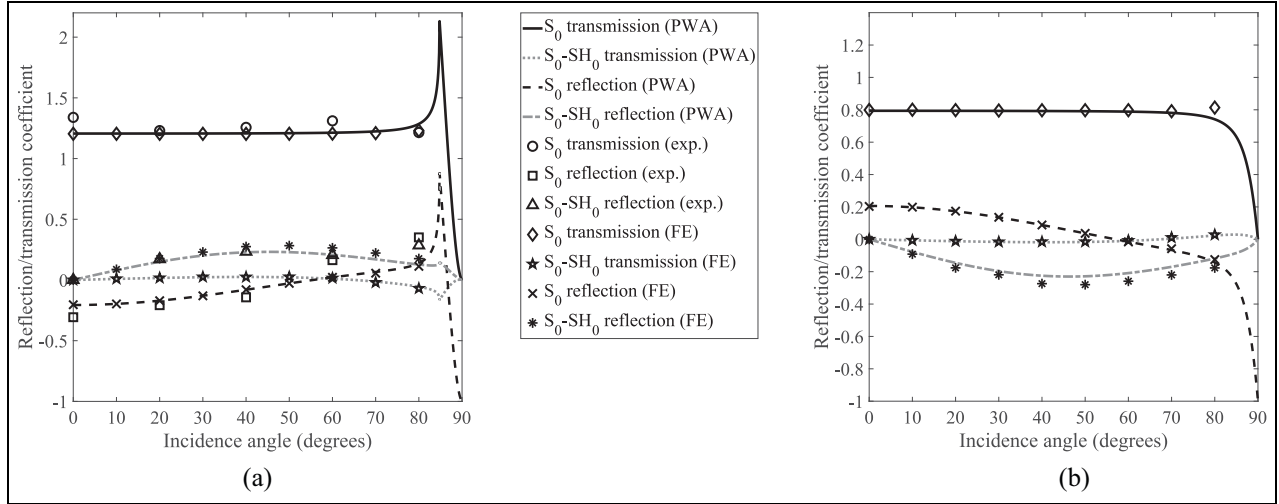


Figure 24. Transmission and reflection coefficients of the studied symmetric modes: (a) AA6061-T6 to AZ31B and (b) AZ31B to AA6061-T6.

$$T_{(S_0 \text{ or } A_0)}^i = \frac{A_{tr}^i(S_0 \text{ or } A_0)}{A_{tr-s}(S_0 \text{ or } A_0)} \quad (11)$$

$$R_{(S_0 \text{ or } A_0)}^i = \frac{A_{refl}^i(S_0 \text{ or } A_0)}{A_{tr-s}(S_0 \text{ or } A_0)} \quad (12)$$

$$T_{(S_0-SH_0)}^i = \frac{A_{tr}^i(S_0-SH_0)}{A_{tr-s}(S_0)} \quad (13)$$

$$R_{(S_0-SH_0)}^i = \frac{A_{refl}^i(S_0-SH_0)}{A_{tr-s}(S_0)} \quad (14)$$

where $T_{(m)}^i$ is the transmission coefficient of mode “ m ” at an incidence angle \hat{i} ; $R_{(m)}^i$ is the reflection coefficient of mode “ m ” at an incidence angle \hat{i} ; $A_{tr}^i(m)$ is the amplitude of the transmitted mode “ m ” after traveling a distance l from Material X to Material Y (incident wave propagating from Material X to Material Y at an angle of incidence \hat{i}); $A_{refl}^i(m)$ is the amplitude of the reflected mode “ m ” after traveling a distance l in Material X (incident wave propagating from Material X to Material Y at an angle of incidence \hat{i}); and $A_{tr-s(m)}$ is the amplitude of the transmitted mode “ m ” after traveling a distance l in a single material (Material X).

Amplitudes of the single-material propagations ($A_{tr-s(m)}$ appearing in the denominators of equations (11) to (14)) can be taken at any incidence angle since there is no material interface. For the FE calculations, it was preferred to take them at the same incidence angle as that of the dissimilar-material propagation (in the numerators) to eliminate the numerical discrepancies that may result from the mesh errors due to wave propagations in different mesh shapes.

To minimize possible errors and variations in the experimental data, and to have only one reference, experimental single-material measurements ($A_{tr-s(m)}$) were taken as an average combining all the tested incidence angles (as mentioned in section “Attenuation curves”). Furthermore, given that the data normalization relied on the third peak of the signal, the calculations of the coefficients were based on the third peak, whenever possible, for consistency.

Transmission and reflection coefficients can be calculated after the wave travels any distance l , as long as l is kept constant between the dissimilar-material and single-material propagations (same l for the numerator and the denominator). For example, the FE transmission coefficient of the S_0 mode can be calculated using the attenuation curves presented in Figure 21, by the division of the value of any blue point (propagation from AA6061-T6 to AZ31B) over the value of its corresponding black point (AA6061-T6 single-material propagation). Calculations should be performed after the wave interacts with the material interface (sensor position >0). Similarly, values from Figure 20 can be used to calculate the experimental transmission coefficient of the S_0 mode. Since experimental data show some perturbation, the transmission coefficient was calculated using all possible data points, then the average value was considered. Figure 20 represents the attenuation curve of the first peak in the S_0 mode; however, coefficients using all other peaks were also calculated, and the peaks with minimal variations were considered. This process was also applied to calculate all the transmission and reflection coefficients of the studied modes. Figures 24 and 25 show the transmission and reflection coefficients of

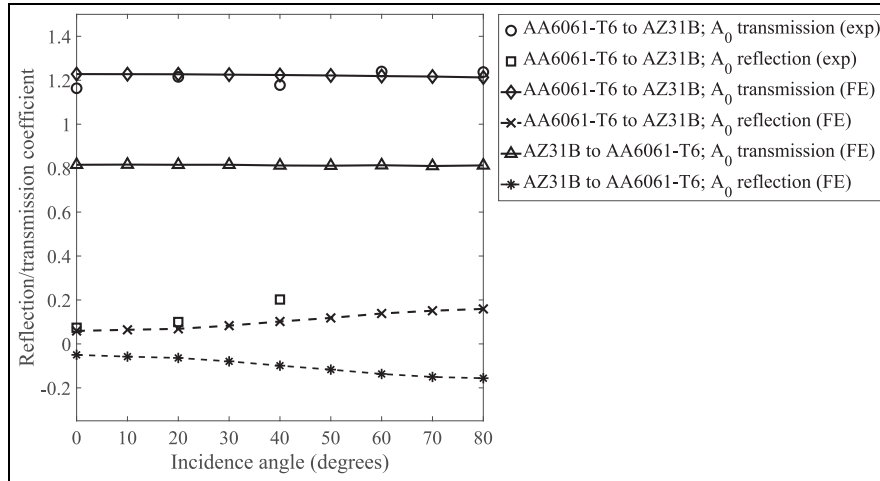


Figure 25. Transmission and reflection coefficients of the A_0 mode.

the symmetric (S_0 and S_0 - SH_0) and anti-symmetric (A_0) wave modes, respectively, for both the forward and the backward propagation directions.

The determination of all experimental coefficients was tedious due to the undesirable superpositions between the anticipated modes and other modes and/or boundary reflections. For this reason, some experimental data points are missing in Figure 25 (AA6061-T6 to AZ31B; A_0 reflection at $\hat{i}=60^\circ$ and $\hat{i}=80^\circ$). In addition, the experimental S_0 - SH_0 transmission coefficients are not available in Figure 24 because the transmission of this mode is extremely weak. The weak amplitude of the S_0 - SH_0 mode is also observed in the FE and PWA results (Figure 24). Furthermore, the experimental results could not be determined for the backward direction because the single-material measurements from the AZ31B plate are not available.

The FE and PWA results are in good agreement. Some variations exist when comparing to the experimental results. The variation is within the acceptable range taking into consideration the sources of errors associated with the PZT placement, material properties, weld condition, and the operational conditions during the testing.

The transmissions of the S_0 and A_0 modes remain approximately constant and unaffected by the change of the incidence angle until it becomes very steep ($\hat{i}\approx 78^\circ$), as can be seen in the experimental, FE, and PWA results. At the S_0 mode's critical angle, a sharp peak appears in the transmission before it drops back to zero. Material properties and excitation frequencies would cause a change in the critical angles of the modes and their interaction behavior; this means that the constant trait among most of the incidence-angle range may not be generalized for other types of materials and other excitation frequencies.

The values of the A_0 and S_0 transmission coefficients are above unity (≈ 1.2 for both modes) when the wave propagates from AA6061-T6 to AZ31B. This means that the amplitude of the propagating wave is amplified by about 20% when it passes from AA6061-T6 to AZ31B. However, the transmission coefficients of the LW modes are about 0.8 when the wave propagates in the opposite direction. Thus, the wave amplitude drops by about 20% when passing from AZ31B to AA6061-T6. This indicates that the wave-field is amplified when passing from a stiff medium to a softer medium, while it is attenuated when the wave's propagation direction is reversed. While energy is conserved, the energy of the wave mode propagating in a soft medium can oscillate the particles with higher amplitude than it can when propagating in a stiffer medium.

The reflection coefficients of the three wave modes (S_0 , A_0 , and S_0 - SH_0) are approximately equal for the forward and backward propagation directions, but they have opposite signs. The opposite signs mean that there is a 180° -phase difference between the reflected modes among the two propagation directions. The similarity in the reflection coefficients, between the two propagation directions, vanishes in the vicinity of the critical angle where sudden sharp peaks appear in the forward direction. Considering the absolute values, the reflection of the A_0 mode has shown a gradual increase with the increase in the incidence angle, with values between 6% and 20% (Figure 25). The reflection of the S_0 mode decreases with the increase in the incidence angle until it reaches zero (at \hat{i} between 55.5° and 57.1°), after which it starts to increase. The reflected S_0 - SH_0 mode increases with the increase in the incidence angle from zero (at $\hat{i}=0^\circ$) up to a certain angle ($\hat{i}\approx 46.5^\circ$), after

which it starts to decrease, with values varying between 0% and 30%.

When an ultrasonic wave encounters a tough interface/medium, the phase of its reflection is expected to change.⁵⁶ This is observed in the results for the AZ31B to AA6061-T6 propagation and is only applicable to the shear modes (negative reflection coefficients for the A_0 and S_0 - SH_0 reflections). On the contrary, the S_0 reflection starts out-of-phase with respect to the shear modes, then it switches the phase in both propagation directions at an incidence angle between 55.5° and 57.1° , after crossing through the point of zero reflection. It was observed that the phase of the S_0 - SH_0 reflection in the FE results was shifted from that of experimental and PWA results, this phase-shift was ignored in the reported findings.

PWA has shown that the maximum S_0 - SH_0 conversion occurs around $\hat{i} \approx 45^\circ$, as was discussed in section "PWA of in-plane modes." FE simulations and experiments were not performed at $\hat{i} = 45^\circ$; however, this result is confirmed by the trend of the FE and experimental results. While the transmitted converted mode is extremely weak, a significant S_0 - SH_0 mode conversion appears as a reflection from the material interface, reaching values of above 20% of the incident-wave amplitude.

Capturing reflections with higher values than what was obtained in this study may indicate the existence of a flaw or damage within the welded AA6061-T6/AZ31B plate. This applies also when capturing transmissions of lower values than the ones that were determined for an intact joint using the same excitation frequency. However, obtaining the same values of reflection and transmission coefficients does not reflect the intact condition of the plate unless proper sensor placement and plate coverage were insured. This can be achieved by performing sensor-network optimization.⁵⁷

It can be noticed that the FE results of the transmitted S_0 mode and the experimental results of the S_0 and S_0 - SH_0 modes are a bit deviated from the PWA results at $\hat{i} = 80^\circ$. The problem at this steep angle is the possible superposition of multiple wave lobes reflecting or transmitting from the weld line due to the wave propagation near the weld. Such superpositions are difficult to separate or identify in the measured signals, which may be the reason for the recorded deviation. In addition, evanescent modes possibly existing near the PZT or the weld line may also interfere with the studied propagating modes.⁵⁰ This is in addition to the fact that this incidence angle is close to the critical angles of both LW modes.

Based on the results presented in this section, mode reflections seem to be highly influenced by the

excitation incidence angle. This fact should be taken into consideration by investigators before using wave reflections for NDE applications. Consequently, reflection-based sensor networks in structures containing an AA6061-T6/AZ31B dissimilar joint could be complex to design and may not be efficient enough. The incidence angles and the amount of reflection expected to emerge from the joint toward each sensor should be taken into consideration while designing or optimizing a sensor network. A stronger reflection means a higher potential of this reflection to carry information about flaws lying between the actuator and the joint or within the joint itself.

On the other hand, Lamb-mode transmissions are almost constant up to a very steep incidence angle ($\hat{i} \approx 78^\circ$) in both the forward and backward propagation directions. This means that transmission-based NDE and sensor networks could be easier to design and use efficiently without considering the complexities of many incident-wave angles.

Concluding remarks

The propagation behavior of the fundamental LW modes, upon the oblique interaction with dissimilar solid mediums, was numerically and experimentally investigated. An intact AA6061-T6/AZ31B joint and non-welded plate(s) were used for this purpose. A technique was developed to identify in-plane and out-of-plane GW modes from the 3D scanning laser vibrometer measurements and the 3D finite element simulations. Reflections from the material interface, as well as the converted S_0 - SH_0 mode's transmissions, were separated from other superpositions appearing in the measured wave-fields. The transmission and reflection coefficients of the studied modes (S_0 , A_0 , and S_0 - SH_0) were assessed and analyzed. The existence of an S_0 - SH_0 mode conversion was verified when an obliquely-incident S_0 mode interacts with the material interface. The transmission of the converted S_0 - SH_0 mode was found to be extremely weak, while the amplitude of its reflection reaches values above 20% of the incident S_0 mode. Reflection amplitudes of the S_0 and A_0 LW modes vary with the incidence angle and reach values up to around 20% of the incident waves. The transmission coefficients of the S_0 and A_0 modes are almost constant, with a variation of less than 5% until a very steep incidence angle ($\hat{i} \approx 78^\circ$). The transmission amplitudes of both modes increase by around 20% when the wave propagates from AA6061-T6 to AZ31B, while it drops by the same percentage in the inverse propagation direction.

The transmission and reflection coefficients of the symmetric modes were accurately predicted using plane-wave analytical solutions. It was confirmed that this approximation can provide good prediction, compared to finite element analysis and experimental investigations, over a range of frequency \times thickness values. The results of this study provide a better understanding of LW interaction with intact dissimilar-material joints.

Acknowledgements

The authors are grateful to the lab assistants at the University of Adelaide in help to perform the experiments, especially Mr Adam Ryntjes. Thanks are extended to Ms Carman Yeung who has helped in using the three-dimensional laser scanner and assisted in running some experiments. The authors also thank Dr Nayla Cortas and Ms Salam Al Hamra at the American University of Beirut-Medical Center (AUBMC) for their help in performing the CT scans.


Declaration of conflicting interests


The author(s) declared no potential conflicts of interest with respect to the research, authorship, and/or publication of this article.


Funding

The authors would like to acknowledge the National Council for Scientific Research of Lebanon (CNRS-L) for granting a doctoral fellowship to (Mohammad Ali Fakh) and for their Award #103085.

ORCID iDs

Mohammad Ali Fakh  <https://orcid.org/0000-0002-2748-8400>

Samir Mustapha  <https://orcid.org/0000-0002-3198-5290>

Ching-Tai Ng  <https://orcid.org/0000-0003-4638-2756>

References

- Li Y, Wei Z, Wang Z, et al. Friction self-piercing riveting of aluminum alloy AA6061-T6 to magnesium alloy AZ31B. *J Manuf Sci E: T ASME* 2013; 135(6): 061007.
- Borrisutthekul R, Miyashita Y and Mutoh Y. Dissimilar material laser welding between magnesium alloy AZ31B and aluminum alloy A5052-O. *Sci Technol Adv Mat* 2005; 6(2): 199–204.
- Liu L, Liu X and Liu S. Microstructure of laser-TIG hybrid welds of dissimilar Mg alloy and Al alloy with Ce as interlayer. *Scripta Mater* 2006; 55(4): 383–386.
- Haghshenas M and Gerlich AP. Joining of automotive sheet materials by friction-based welding methods: a review. *Eng Sci Technol* 2018; 21(1): 130–148.
- Liu L, Wang H, Song G, et al. Microstructure characteristics and mechanical properties of laser weld bonding of magnesium alloy to aluminum alloy. *J Mater Sci* 2007; 42(2): 565–572.
- Thomas WM, Nicholas ED, Needham JC, et al. *Friction stir butt welding*. GB Patent 9125978 8, 1991.
- Thomas WM, Nicholas ED, Needham JC, et al. *Improvements relating to friction welding*. US Patent 5 460 317; EPS 0 616 490, 1991.
- Burford D, Widener C and Tweedy B. Advances in friction stir welding for aerospace applications. In: *Proceedings of the 6th AIAA aviation technology, integration and operations conference (ATIO)*, Wichita, KS, 25–27 September 2006, p. 7730. Reston, VA: AIAA.
- Fakh MA, Mustapha S, Tarraf J, et al. Detection and assessment of flaws in friction stir welded joints using ultrasonic guided waves: experimental and finite element analysis. *Mech Syst Signal Pr* 2018; 101: 516–534.
- Gite RA, Loharkar PK and Shimpi R. Friction stir welding parameters and application: a review. *Mater Today: Proc* 2019; 19: 361–365.
- Gholizadeh S. A review of non-destructive testing methods of composite materials. *Proced Struct Integ* 2016; 1: 50–57.
- Harb MS and Yuan F-G. Barely visible impact damage imaging using non-contact air-coupled transducer/laser Doppler vibrometer system. *Struct Health Monit* 2017; 16(6): 663–673.
- Harb MS and Yuan F-G. Air-coupled nondestructive evaluation dissected. *J Nondestruct Eval* 2018; 37(3): 50.
- Mustapha S and Ye L. Leaky and non-leaky behaviours of guided waves in CF/EP sandwich structures. *Wave Motion* 2014; 51(6): 905–918.
- Mustapha S and Ye L. Propagation behaviour of guided waves in tapered sandwich structures and debonding identification using time reversal. *Wave Motion* 2015; 57: 154–170.
- Yeung C and Ng C-T. Time-domain spectral finite element method for analysis of torsional guided waves scattering and mode conversion by cracks in pipes. *Mech Syst Signal Pr* 2019; 128: 305–317.
- Su Z and Ye L. *Identification of damage using Lamb waves: from fundamentals to applications*. London: Springer Science + Business Media, 2009.
- Su Z, Ye L and Lu Y. Guided Lamb waves for identification of damage in composite structures: a review. *J Sound Vib* 2006; 295(3–5): 753–780.
- Fakh MA, Mustapha S and Abdul-Aziz A. Robust localization and classification of barely visible indentations in composite structures by fusion of ultrasonic damage indices. *J Nondestruct Eval Diagn Prog Eng Syst* 2019; 2(3): 031004.
- Staszewski WJ, Lee BC and Traynor R. Fatigue crack detection in metallic structures with Lamb waves and 3D laser vibrometry. *Meas Sci Technol* 2007; 18(3): 727.
- Yang Y, Ng C-T and Kotousov A. Influence of crack opening and incident wave angle on second harmonic generation of Lamb waves. *Smart Mater Struct* 2018; 27(5): 055013.
- Pan N, Su Z, Ye L, et al. A quantitative identification approach for delamination in laminated composite beams using digital damage fingerprints (DDFs). *Compos Struct* 2006; 75(1–4): 559–570.

23. Pudipeddi GT, Ng C-T and Kotousov A. Mode conversion and scattering of Lamb waves at delaminations in composite laminates. *J Aerospace Eng* 2019; 32(5): 04019067.
24. Mustapha S, Ye L, Dong X, et al. Evaluation of barely visible indentation damage (BVID) in CF/EP sandwich composites using guided wave signals. *Mech Syst Signal Pr* 2016; 76: 497–517.
25. Mustapha S, Ye L, Wang D, et al. Debonding detection in composite sandwich structures based on guided waves. *AIAA J* 2012; 50(8): 1697–1706.
26. Yang Y, Ng C-T and Kotousov A. Second harmonic generation of guided wave at crack-induced debonding in FRP-strengthened metallic plates. *Int J Struct Stab Dy* 2019; 19(1): 1940006.
27. Aryan P, Kotousov A, Ng C-T, et al. A baseline-free and non-contact method for detection and imaging of structural damage using 3D laser vibrometry. *Struct Control Hlth* 2017; 24(4): e1894.
28. Harb MS and Yuan F-G. Damage imaging using non-contact air-coupled transducer/laser Doppler vibrometer system. *Struct Health Monit* 2016; 15(2): 193–203.
29. Rathod VT and Mahapatra DR. Ultrasonic Lamb wave based monitoring of corrosion type of damage in plate using a circular array of piezoelectric transducers. *NDT&E Int* 2011; 44(7): 628–636.
30. Hamade RF, Fakih MA, Harb MS, et al. Quality assessment of friction stir welded joints—using the fundamental anti-symmetric Lamb wave mode. *Mater Sci Forum* 2018; 941: 2429–2434.
31. Tarraf J, Mustapha S, Fakih MA, et al. Application of ultrasonic waves towards the inspection of similar and dissimilar friction stir welded joints. *J Mater Process Tech* 2018; 255: 570–583.
32. Wilcox PD, Velichko A, Drinkwater BW, et al. Scattering of plane guided waves obliquely incident on a straight feature with uniform cross-section. *J Acoust Soc Am* 2010; 128(5): 2715–2725.
33. Sondhauss C. XIV. *On the refraction of sound. Lond Edinbur Dublin Philos Mag J Sci* 1853; 5(30): 73–77.
34. Knott CG. III. Reflexion and refraction of elastic waves, with seismological applications. *Lond Edinbur Dublin Philos Mag J Sci* 1899; 48(290): 64–97.
35. Zoeppritz K. On the reflection and propagation of seismic waves. *Gott Nachr* 1919; 1(5): 66–84.
36. Blut H. Contribution to the theory of reflection and refraction of elastic waves from layers of discontinuity. *Zeitschr Geophys* 1932; 8(3): 130–144.
37. McCamy K, Meyer RP and Smith TJ. Generally applicable solutions of Zoeppritz' amplitude equations. *B Seismol Soc Am* 1962; 52(4): 923–955.
38. Ergin K. Energy ratio of the seismic waves reflected and refracted at a rock-water boundary. *B Seismol Soc Am* 1952; 42(4): 349–372.
39. Mayer WG. Energy partition of ultrasonic waves at flat boundaries. *Ultrasonics* 1965; 3(2): 62–68.
40. Cheeke JDN. *Fundamentals and applications of ultrasonic waves*. Boca Raton, FL: CRC Press, 2016.
41. Rose JL. *Ultrasonic guided waves in solid media*. Cambridge: Cambridge University Press, 2014.
42. Gregory RD and Gladwell I. The reflection of a symmetric Rayleigh-Lamb wave at the fixed or free edge of a plate. *J Elasticity* 1983; 13(2): 185–206.
43. Scandrett C and Vasudevan N. The propagation of time harmonic Rayleigh-Lamb waves in a bimaterial plate. *J Acoust Soc Am* 1991; 89(4): 1606–1614.
44. Gunawan A and Hirose S. Reflection of obliquely incident guided waves by an edge of a plate. *Mater Trans* 2007; 48(6): 1236–1243.
45. Santhanam S and Demirli R. Reflection of Lamb waves obliquely incident on the free edge of a plate. *Ultrasonics* 2013; 53(1): 271–282.
46. Shen Y and Giurgiutiu V. WFR-2D: an analytical model for PWAS-generated 2D ultrasonic guided wave propagation. In: *Proceedings of the SPIE health monitoring of structural and biological systems*, San Diego, CA, 9–13 March 2014, vol. 9064, p. 906411. Bellingham, WA: SPIE, the International Society for Optics and Photonics.
47. Poddar B and Giurgiutiu V. Scattering of Lamb waves from a discontinuity: an improved analytical approach. *Wave Motion* 2016; 65: 79–91.
48. Haider MF, Bhuiyan MY, Poddar B, et al. Analytical and experimental investigation of the interaction of Lamb waves in a stiffened aluminum plate with a horizontal crack at the root of the stiffener. *J Sound Vib* 2018; 431: 212–225.
49. Fakih MA, Mustapha S and Harb MS. The interaction of the fundamental symmetric and antisymmetric Lamb wave modes with material discontinuity—a 3D finite element analysis. In: *Proceedings of the 7th Asia-Pacific workshop on structural health monitoring (APWSHM)*, Hong Kong SAR, P.R. China, 12–15 November 2018.
50. Giurgiutiu V. *Structural health monitoring with piezoelectric wafer active sensors*. Amsterdam: Elsevier, 2007.
51. Laboratory for Active Materials and Smart Structures (LAMSS). *Wavescope 2.5: dispersion curves, group velocities, and tuning for metallic structures*. University of South Carolina. MATLAB-based software, 2010. Retrieved from <http://www.me.sc.edu/Research/lamss/html/software.html>
52. Su Z, Yang C, Pan N, et al. Assessment of delamination in composite beams using shear horizontal (SH) wave mode. *Compos Sci Technol* 2007; 67(2): 244–251.
53. Callister WD and Rethwisch DG. *Materials science and engineering*. New York: John Wiley & Sons, 2011.
54. Krautkramer J and Krautkramer H. *Ultrasonic testing of materials*. New York; Berlin; Heidelberg: Springer-Verlag, 1990.
55. Wilcox P, Lowe M and Cawley P. Mode and transducer selection for long range Lamb wave inspection. *J Intel Mat Syst Str* 2001; 12(8): 553–565.
56. Azhari H. *Basics of biomedical ultrasound for engineers*. Hoboken, NJ: John Wiley & Sons, 2010.
57. Ismail Z, Mustapha S, Fakih MA, et al. Sensor placement optimization on complex and large metallic and composite structures. *Struct Health Monit* 2020; 19(1): 262–280.